Search for Unparticles in the Z + MET channel with the CMS Experiment at $\sqrt{s} = 8$ TeV

von

Lars Daniel Reusch

Diplomarbeit in Physik

vorgelegt der

Fakultät für Mathematik, Informatik und Naturwissenschaften
der Rheinisch-Westfälischen Technischen Hochschule Aachen

im Oktober 2013

angefertigt im

III. Physikalischen Institut A
Prof. Dr. Thomas Hebbeker

Zweitgutachter
Prof. Dr. Christopher Wiebusch

Zusammenfassung

In der Teilchenphysik gibt es viele Vorschläge, wie man das Standardmodell erweitern könnte. Die meisten Theorien postulieren dazu neue Teilchen. So wird z.B. in der Supersymmetrie jedem Teilchen ein Superpartner zugeordnet und damit die Teilchenanzahl verdoppelt. Die Unparticle Theorie dagegen sagt keine neuen Teilchen im traditionellen Sinn voraus. Stattdessen schlug H. Georgi 2007 [1] vor, dass die Wechselwirkung eines "konformen" Feldes mit dem Standardmodellfeld bei sehr hohen Energien zu "unparticle stuff" bei niedrigeren (im Experiment beobachtbaren) Energien führen könnte. Wegen ihrer kontinuierlichen Massenverteilung unterscheiden sich Unparticles wesentlich von gewöhnlichen Teilchen.

In dieser Arbeit wird in den im Jahr 2012 vom CMS Experiment aufgenommenen Daten, die $19.7\,\mathrm{fb}^{-1}$ entsprechen, nach Anzeichen von Unparticles gesucht. Speziell im Kanal mit einem Z Boson und fehlender transversaler Energie wird die Analyse durchgeführt, da als Signal die assozierte Produktion von einem Unparticle und einem Z-Boson angenommen wird. Das Z zerfällt anschließend leptonisch, aber das Unparticle verlässt den Detektor ungesehen. Ein möglicher indirekter Nachweis kann daher nur über die fehlende transversale Energie erfolgen.

Um Untergrundprozesse mit sehr ähnlicher Signatur besser vom Signal unterscheiden zu können, werden Selektionsschnitte angewendet. Diese sind darauf ausgelegt den Untergrund möglichst effektiv zu unterdrücken und gleichzeitig auf eine hohe Signaleffizienz zu achten. Außerdem werden die systematischen Unsicherheiten auf die Vorhersagen für Signal und Untergrund untersucht.

Da sich kein signifikanter Überschuß an Daten im Vergleich zu den Untergründen zeigt, werden obere Ausschlußgrenzen für den Wirkungsquerschnitt des Signals berechnet. Die Ausschlussgrenzen von vergleichbaren Untersuchungen können dabei leicht verbessert werden.

Abstract

In particle physics, there are many proposals how to expand the Standard Model. Most of those theories postulate new particles. Supersymmetry e.g. pairs every particle with a superpartner, effectively doubling the number of particles. The unparticle theory however does not predict new particles in the traditional sense. Instead H. Georgi proposed in 2007 [1] that the interaction of a conformal field with the Standard Model field at very high energies could lead to "unparticle stuff" at lower (experimentally observable) energies. Because of their continuous mass distribution unparticles are not particles in the common sense.

In this thesis, a search for unparticles is conducted on the $19.7\,\mathrm{fb}^{-1}$ of data taken by the CMS experiment in 2012. The analysis is performed in the channel with a Z boson and missing transverse energy, because the signal is the associated production of an unparticle and a Z boson. The Z then decays into two leptons and the unparticle leaves the detector unseen. Therefore, evidence can only be found by considering the missing transverse energy.

To better discriminate background processes with a very similar signature from the signal, certain cuts are applied. They are designed to effectively suppress the background while ensuring a high signal efficiency. Furthermore, the systematic uncertainties on signal and background are investigated.

As data and background are in good agreement, upper exclusion limits on the signal cross section are calculated. Limits of comparable experiments can be slightly enhanced.

Contents

1. Introduction

Curiosity is probably one of the most important human traits. It is what prompts us to explore the world and find out how things work. Careful observations eventually lead to an accurate description of any puzzling phenomenon. Then, the scientific approach is to formulate a theory and make unique predictions that can be tested in experiments. We have come a long way in explaining our world in such a manner.

The Standard Model (SM) of particle physics gives a very good description of the elementary building blocks and how they construct all the matter that we see around us. 6 quarks, 6 leptons and some additional particles mediating the electromagnetic, weak, and strong force is about all it takes. Many tests and the discoveries of predicted particles support the SM. Just last year, two experiments at the Large Hadron Collider (LHC) have found the Higgs particle that evaded discovery for many years and is essential in explaining the mass of the particles. This success gives rise to the question, why we should look at physics beyond the Standard Model. The answer is, there are still unresolved issues: e.g. gravitation, the forth and most noticeable force, can not be formulated as a quantum field theory like the other three. There is also an indication that the matter we can describe makes up only 4 % of all matter and energy in the universe.

In an effort to address the shortcomings of the SM, many new theories or SM extensions have been proposed. Preferably, a new theory makes only very few assumptions, is easy to test and can potentially explain many of the open issues.

One such theory was introduced by H. Georgi [1] and others in 2007. A scale-invariant field couples to the SM field in a hidden sector at a high energy scale. The resulting effective theory at a lower (and observable) scale leads to a single new particle with only four free parameters and the peculiarity of a continuous mass spectrum. Because of this distinct difference to all the other particles, it is called unparticle. Many theorists have investigated different unparticle couplings to SM particles and the Higgs boson, rendering the unparticle a possible candidate for dark matter or even an Unhiggs.

In this thesis, the search for unparticles from the associated production with Z bosons at the Compact Muon Solenoid experiment at the LHC with data taken in 2012 is presented.

2. Theoretical Foundations

In this first chapter, a short introduction to the Standard Model of particle physics is presented. Including some known issues the theory fails to explain. Then the unparticle theory and its implications are described to motivate the analysis performed in this thesis.

2.1. The Standard Model

The Standard Model (SM) is a theory that very successfully describes the known particles and their interactions. Many SM predictions have been confirmed in countless experiments over the years. Most recently the discovery of a new boson (the Higgs) at the Large Hadron Collider further consolidated the confidence in the theory. Yet, there are still unresolved questions that motivate the search beyond the Standard Model.

In the following sections, a description of the particle structure and of three of the four fundamental forces that can be explained within the Standard Model will be given based on [2].

2.1.1. Particles

One of the beautiful aspects of the Standard Model is that the hundreds of particles in the so called particle zoo can all be built from just a few elementary particles. There are only 6 leptons, 6 quarks and the mediators of the interactions. Both leptons and quarks can be classified into 3 generations as shown in fig. 2.1.

All elementary particles are assumed to be pointlike, their properties include mass m, charge Q, spin s and further quantum numbers. Leptons have lepton numbers according to their generation and each quark has its own flavor. Additionally, the quarks come in 3 different colors. There are also 6 antileptons and 6 antiquarks, where the sign of the charge and the lepton number or flavor is reversed.

The gauge bosons (explained below) are the mediators of the interactions: the photon

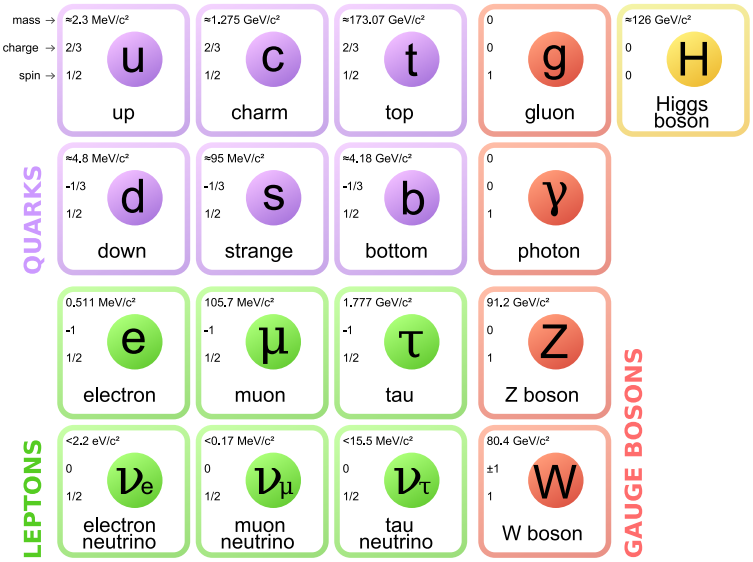

Figure 2.1.: Elementary particles of the Standard Model [3]. The first 3 columns denote the 1st, 2nd and 3rd generation. The charges are given in units of the electron charge e. The masses are taken from [4].

for the electromagnetic force, W^+,W^- and Z for the weak force and 8 gluons carrying color charge for the strong force.

2.1.2. Field Theory

In quantum field theory, the idea is to describe interactions as fields that occupy a region of space, whereas a particle is localized. Field variables $\phi_i(x, y, z, t)$ can represent any physical property as function of position and time. Analogous to the Lagrangian $L(q_i, \dot{q}_i)$ in classical mechanics describing the particle motion, field theory introduces a Lagrangian density $\mathcal{L}$ that is a function of the fields ϕ_i and their derivatives $\partial_\mu \phi_i$. Inserting a Lagrangian $\mathcal{L}$ into the Euler-Lagrange equation

$$\partial_\mu \left(\frac{\partial \mathcal{L}}{\partial(\partial_\mu \phi_i)} \right) = \frac{\partial \mathcal{L}}{\partial \phi_i} \tag{2.1}$$

results in an equation of motion for a particle described by field ϕ_i.

A Lagrangian is invariant under the global phase transformation

$$\psi \rightarrow e^{i\theta}\psi, \tag{2.2}$$

but not under a local phase transformation

$$\psi \rightarrow e^{i\theta(x)}\psi \tag{2.3}$$

as new terms are added due to the derivatives of $\theta(x)$. Demanding local gauge invariance, because there is no reason why global invariance should not hold locally, requires a modification of the complete Lagrangian by adding new field terms. Surprisingly, the new field then describes the gauge boson of the considered interaction.

2.1.3. Electromagnetic Force

The free Dirac Lagrangian for a spinor (spin-$\frac{1}{2}$) field ψ is used as a starting point to describe the electromagnetic interaction in Quantum Electro Dynamics (QED). When applying the modifications to achieve local gauge invariance the Lagrangian reads:

$$\mathcal{L} = \left[i\bar{\psi}\gamma^{\mu}\partial_{\mu}\psi - m\bar{\psi}\psi\right] - \left[\frac{1}{16\pi}F^{\mu\nu}F_{\mu\nu}\right] - (q\bar{\psi}\gamma^{\mu}\psi)A_{\mu}, \tag{2.4}$$

with $F^{\mu\nu} = \partial^{\mu}A^{\nu} - \partial^{\nu}A^{\mu}$. The first term is the free Lagrangian and the third introduces a massless vector (spin-1) field A^{μ}, which is the electromagnetic potential. The photon is the massless particle that mediates the electromagnetic force between charged particles.

The global phase transformation is the same as a multiplication of ψ by a unitary 1×1 matrix $U = e^{i\theta}$. The group $U(1)$ contains all of those unitary matrices and the $U(1)$ gauge invariance denotes the symmetry in the transformations. This principle can be extended to the group $SU(2)$ for the weak interaction, as well as to $SU(3)$ in Quantum Chromo Dynamics.

2.1.4. Strong Force

As mentioned before, all quarks can have three different colors: red, blue and green. Formulating the Lagrangian for a single flavor, one has to take the possible colors into account. By combining the three Dirac spinors into a vector:

$$\psi = \begin{pmatrix}\psi_r \\ \psi_b \\ \psi_g\end{pmatrix}, \bar{\psi} = (\bar{\psi}_r\bar{\psi}_b\bar{\psi}_g) \tag{2.5}$$

the free Lagrangian takes the form of the one-particle Dirac Lagrangian of the electromagnetic interaction:

$$\mathcal{L} = i\bar{\psi}\gamma^{\mu}\partial_{\mu}\psi - m\bar{\psi}\psi. \tag{2.6}$$

When $SU(3)$ color symmetry is applied, the resulting Lagrangian (invariant under local $SU(3)$ gauge transformation) contains 8 massless vector fields corresponding to the gluons that propagate the strong force between colored particles, the quarks. The gluons can also interact with themselves.

Quarks only appear in bound states. Combinations of two or three quarks bound by the strong force form heavier particles called hadrons. They are always color neutral. Mesons consist of a quark of a certain color and an antiquark of the corresponding anticolor and baryons are built from three (anti)quarks of different (anti)color.

2.1.5. Weak Force

The weak interaction is connected to the quark flavor or to the generation of the leptons. All leptons and quarks take part in it. The interaction can be neutral (mediated by the neutral Z) or charged (by exchange of the two $W^{\pm}$).

The charged bosons W^+ and W^- only couple to left-handed fermions. The group $SU(2)_L$ is used with the weak isospin I. Local gauge invariance leads to three new massless bosons W^1_μ,W^2_μ and W^3_μ. While linear combinations of the first two result in the observed charged bosons:

$$W^{\pm}_\mu = \frac{1}{\sqrt{2}}(W^1_\mu \mp W^2_\mu), \tag{2.7}$$

the third does not match to the Z boson.

In the GWS[1] model, the gauge group is expanded to $SU(2)_L \times U(1)$, unifying the weak and electromagnetic interactions. This results in an additional boson B_μ, which combined with W^3_μ leads to

$$A_\mu = B_\mu \cos\theta_w + W^3_\mu \sin\theta_w \tag{2.8}$$

$$Z_\mu = -B_\mu \sin\theta_w + W^3_\mu \cos\theta_w, \tag{2.9}$$

where A_μ is the photon and Z_μ the Z boson. The mixing or Weinberg angle θ_w is a free parameter.

2.1.6. The Higgs Mechanism

As seen in the previous sections, local gauge invariance can explain the mediator particles of three fundamental forces. However, their gauge fields have to be massless.

[1] Glashow Weinberg Salam

The photon and the gluons are indeed found to have no mass, but the Z and the Ws are massive particles. Adding a mass term to the Lagrangian of the weak interaction, would break the local gauge symmetry. To solve this problem, spontaneous symmetry-breaking and the Higgs mechanism are introduced. Using the complex field:

$$\phi = \phi_1 + i\phi_2, \tag{2.10}$$

a Lagrangian with the real fields ϕ_1 and ϕ_2 that is spontaneously breaking the symmetry can be rewritten as

$$\mathcal{L} = \frac{1}{2}(\partial_\mu \phi)^\star (\partial^\mu \phi) + \frac{1}{2}\mu^2(\phi^\star \phi) - \frac{1}{4}\lambda^2(\phi^\star \phi)^2. \tag{2.11}$$

In this notation, it is invariant under U(1) phase transformation. Applying local gauge symmetry results in the desired massive gauge field A^μ and another single massive scalar, called the Higgs boson. Interaction with this Higgs field is what gives particles their mass.

2.1.7. Shortcomings of the Standard Model

Despite the success of the Standard Model with its predictions leading to the discovery of new particles (e.g. the top quark in 1995 and the Higgs in 2012), there are still some unresolved issues. A few examples are given below:

- Dark matter:
  In astronomy, measurements of the rotation velocity of galaxies and calculations of the gravitational effects indicate that the universe contains significantly more matter than is actually visible. The matter described in the Standard Model only accounts for about 5 % of the entire mass and energy. The remaining matter, which is not radiating and hence called dark matter, makes up about 20 %. The rest is assumed to be dark energy. Possible candidates for dark matter are Weakly Interacting Massive Particles (WIMPs) that need to be stable, neutral and have a considerable mass. The Standard Model does not contain such particles.
- Grand Unified Theory:
  Just as the electromagnetic and weak interaction can be unified in the electroweak force explaining the Z and Ws, efforts are made to also include the strong force to form a Grand Unified Theory (GUT). The idea is that all three forces could be the result of a single underlying force and at a higher energy scale ($\approx 10^{16}$ GeV) the three coupling constants, dependent on the energy scale, would have the same strength. However, the three coupling constants do not meet exactly in a single point in the Standard Model.

Another issue with the unification of the forces is that there is still no quantum theory of gravitation, the remaining fundamental force. As with the other forces, such a theory could result in a new mediator particle for the gravitational force. This hypothetical gauge boson is called graviton.

- Hierarchy Problem and Fine Tuning:
  The reason why there is such a big difference in the masses of the elementary particles between the generations or why the fundamental forces differ in strength several orders of magnitude can not be given by the theory. It is referred to as hierarchy problem. It also occurs when considering the Higgs mass M_H:

$$M_H^2 = M_0^2 - \frac{|\lambda_f|^2}{8\pi^2}\Lambda^2 + \dots \tag{2.12}$$

  The required correction term due to possible fermion loops contains an energy cut off parameter Λ. At an energy scale of $\Lambda \approx 10^{16}\,\text{GeV}$, the uncorrected Higgs mass M_0 has to be determined to a very high precision to get the expected result of $M_H \approx 126\,\text{GeV}$. A theory that does not require such a fine tuning of the natural constants would be much more satisfying.

2.2. Beyond the Standard Model

The previous sections showed that the Standard Model provides a very good description of the particle world, but there is also room for expansions and new theories. In the following, one possible approach to new physics is described.

2.2.1. Conformal Fields

Conformal Field Theory (CFT) is a quantum theory which is invariant under conformal transformations. Such transformations introduce a conservation of angles between curves. Apart from that conformal fields are also scale-invariant. This means CFT can be used to study scale-invariant theories. Though it has to be noted that scale-invariant models do not necessarily comply to the conformal invariance. As for the unparticle theory, conformal invariance is not strictly required, but as shown in [5] a non-conformal scale-invariant unparticle would cause novel effects in Standard Model processes due to oscillations of correlation functions.

2.2.2. Unparticle Theory

In the unparticle theory [1, 6, 7], it is proposed that scale-invariant fields with a non-trivial infrared fixed point, called Banks-Zaks ($\mathcal{BZ}$) fields, interact with the Standard Model field through the exchange of very heavy particles at a hidden mass scale $M_{\mathcal{U}}$. Below that scale, the interaction can be described by nonrenormalizable couplings which are suppressed by powers of $M_{\mathcal{U}}$:

$$\mathcal{L}_{int} = \frac{1}{M_{\mathcal{U}}^{k}} O_{SM} O_{\mathcal{BZ}}, \tag{2.13}$$

where O_{SM} and $O_{\mathcal{BZ}}$ are operators of the Standard Model and the $\mathcal{BZ}$ fields respectively. Expressing the exponent in term of the field operator dimensions d_{SM} and $d_{\mathcal{BZ}}$, leads to $k = d_{\mathcal{BZ}} + d_{SM} - 4$.

Moving to lower energies at a scale $\Lambda_{\mathcal{U}}$, the scale-invariance of the $\mathcal{BZ}$ fields emerges and the renormalization couplings cause dimensional transmutation. In an effective field theory below the energy scale $\Lambda_{\mathcal{U}}$, the interaction term of the Lagrangian can be written as:

$$\mathcal{L}_{int}^{eff} = C_{\mathcal{U}} \frac{\Lambda_{\mathcal{U}}^{d_{\mathcal{BZ}} - d_{\mathcal{U}}}}{M_{\mathcal{U}}^{d_{\mathcal{BZ}} + d_{SM} - 4}} O_{SM} O_{\mathcal{U}}, \tag{2.14}$$

where the operators $O_{\mathcal{BZ}}$ of the $\mathcal{BZ}$ fields match onto unparticle operators $O_{\mathcal{U}}$ of dimension $d_{\mathcal{U}}$. $C_{\mathcal{U}}$ is a constant coefficient function. The coupling between the Standard Model and unparticles is represented by:

$$\lambda = C_{\mathcal{U}} \frac{\Lambda_{\mathcal{U}}^{d_{\mathcal{BZ}} - d_{\mathcal{U}}}}{M_{\mathcal{U}}^{d_{\mathcal{BZ}} + d_{SM} - 4}}. \tag{2.15}$$

Phase Space

The scale invariance in the effective theory can be used to fix the two-point functions. For a scalar unparticle operator, the two-point function is [8]:

$$\begin{aligned} \langle 0|O_{\mathcal{U}}(x) O_{\mathcal{U}}^{\dagger}(0)|0\rangle &= \langle 0|e^{i\hat{P}\cdot x} O_{\mathcal{U}}(0) e^{-i\hat{P}\cdot x} O_{\mathcal{U}}^{\dagger}(0)|0\rangle \\ &= \int d\lambda \int d\lambda' \langle 0|O_{\mathcal{U}}(0)|\lambda'\rangle \langle \lambda'|e^{-i\hat{P}\cdot x}|\lambda\rangle \langle \lambda|O_{\mathcal{U}}^{\dagger}(0)|0\rangle \\ &= \int \frac{d^4P}{(2\pi)^4} e^{-iP\cdot x} \rho_{\mathcal{U}}(P^2), \end{aligned} \tag{2.16}$$

where the spectral density $\rho_{\mathcal{U}}(P^2)$ is given by:

$$\rho_{\mathcal{U}}(P^2) = A_{d_{\mathcal{U}}} \theta(P^0) \theta(P^2) (P^2)^{d_{\mathcal{U}} - 2}, \tag{2.17}$$

with the invariant unparticle mass P, the Heaviside function θ and the normalization factor $A_{d_\mathcal{U}}$:

$$A_{d_\mathcal{U}} = \frac{16\pi^{5/2}}{(2\pi)^{2d_\mathcal{U}}} \frac{\Gamma(d_\mathcal{U} + \frac{1}{2})}{\Gamma(d_\mathcal{U} - 1)\Gamma(2d_\mathcal{U})}. \tag{2.18}$$

In this form, the spectral density resembles the phase space for $d_\mathcal{U}$ massless particles. As the unparticle dimension does not have to be integer, the unparticle could be viewed as a fractional number of particles.

Theoretically, the unparticle model could be viewed as a special case of the HEIDI model [**?**] where the Standard Model is extended with singlet fields. These singlet fields can live in higher dimensions d, which can be fractional just like the unparticle dimension $d_\mathcal{U}$.

Matrix Element

The matrix element for the process $f\bar{f} \to Z\mathcal{U}$, which is studied in this analysis, is given by [9]:

$$|\bar{\mathcal{M}}|^2 = \frac{1}{4N_c} \left(\frac{e^2}{\sin^2\theta_W \cos^2\theta_W} \right) (g_{L,q}^2 + g_{R,q}^2)\lambda^2 |A|^2, \tag{2.19}$$

with the electroweak specific factors $g_{L,d} = -\frac{1}{2} + \frac{1}{3}\sin^2\theta_W$, $g_{R,d} = +\frac{1}{3}\sin^2\theta_W$, $g_{L,u} = \frac{1}{2} - \frac{2}{3}\sin^2\theta_W$ and $g_{R,u} = -\frac{2}{3}\sin^2\theta_W$. $|A|^2$ contains the kinematics. The Mandelstam variables s, t and u are used:

$$\begin{aligned} |A|^2 =& 4 \left[-\frac{s}{t} - \left(1 - \frac{m_Z^2}{t}\right)\left(1 - \frac{P_\mathcal{U}^2}{t}\right) - \frac{s}{u} \right. \\ & \left. - \left(1 - \frac{m_Z^2}{u}\right)\left(1 - \frac{P_\mathcal{U}^2}{u}\right) + 2\left(1 - \frac{P_\mathcal{U}^2}{t}\right)\left(1 - \frac{P_\mathcal{U}^2}{u}\right) \right], \end{aligned} \tag{2.20}$$

where m_Z is the Z mass and $P_\mathcal{U}$ is the invariant unparticle mass, $0 \leq P_\mathcal{U}^2 \leq (\sqrt{s} - m_Z)^2$.

Unparticle Spin

The spin of the unparticle is a free parameter in the theory. Investigating the coupling of the Standard Model and CFTs [10], lower bounds on the dimension $d_\mathcal{U}$ are found due to unitarity. Those bounds depend on the spins of the operator fields. Table 2.1 lists the minimal dimension $d_\mathcal{U}$ for different unparticle spins. In this analysis only scalar unparticles are considered. With a lower bound of $d_\mathcal{U} \geq 1$, they have the highest cross section (cf. equation 5.2) which increases the potential for discovery.

spin	0	1/2	1	2
$d_{\mathcal{U},min}$	1	3/2	3	4

Table 2.1.: Lower bounds on the unparticle dimension depending on its spin.

Unparticle Coupling

The process chosen for the analysis is the associated production of a Z boson and an unparticle. The Feynman diagrams in fig. 2.2 show the possible couplings of the unparticle to Standard Model particles in this production channel. The unparticle coupling strength λ is not determined by the theory and could vary between the Z and the quarks. For simplicity, a coupling of equal strength to all Standard Model particles is assumed.

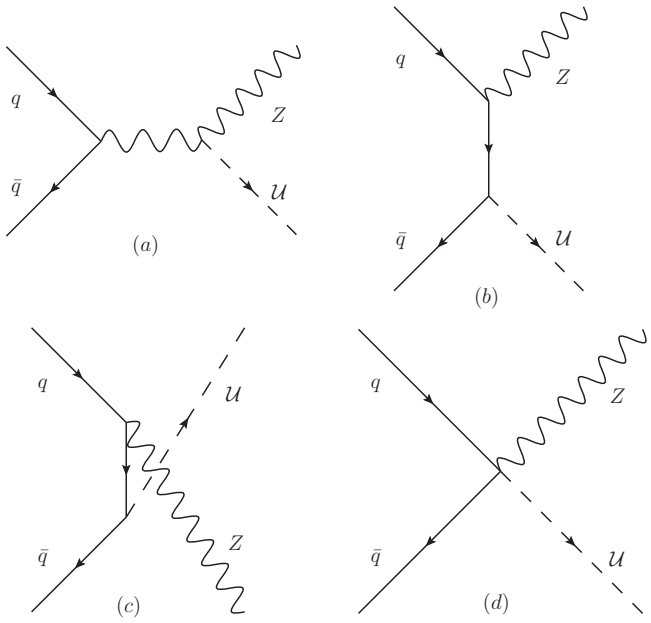

Figure 2.2.: Feynman diagrams of possible associated productions of Z and $\mathcal{U}$ in LO.

2.2.3. Aspects of the Unparticle Model

The following short sections are intended to show the variety of theoretical considerations on the unparticle model and its implications.

Higgs Coupling

A possible coupling of the unparticle to the Higgs boson is investigated in [11]. As a result, the Higgs mass and its width would change and the Higgs would no longer be observed at the mass that the Standard Model predicts.

[12] proposes that the unparticle itself could be viewed as Higgs or rather Unhiggs. All the indications of a Higgs boson could be explained with the Unhiggs.

Another coupling is proposed in [13]. By introducing a $\mathbb{Z}_2$ parity, where unparticles are odd and SM particles are even, the unparticle becomes stable and can couple to the SM Higgs doublet. Associating with the electroweak symmetry breaking, the unparticle obtains mass and becomes a WIMP dark matter candidate.

Mass Gap

When the conformal symmetry is broken, the standard way to handle it, is to introduce a mass gap in the spectral density [14]. It can be a gap of several GeV. The SM Higgs, acquiring a vacuum expectation value, introduces a large breaking of the conformal invariance. The corresponding mass gap can have effects in the cosmology and phenomenology of unparticles [15].

Unparticle Self-interaction

Self-interactions of the unparticle could, according to [16], lead to interesting collider signals with cross sections of pb at the LHC. The 3-point interaction $\mathcal{U} \to \mathcal{U}\mathcal{U}$ with unstable unparticles could e.g. result in $\gamma\gamma\gamma\gamma$, $4l$ or $\gamma\gamma ZZ$. However, [17] shows that strong unitarity bounds on multi-photon events can be obtained, when requiring conformal invariance. The cross sections have to be below 200 fb.

3. Experimental Setup

The data used in this analysis has been recorded by the CMS experiment at the Large Hadron Collider during the runs of 2012. This chapter gives an overview of the collider, the CMS detector and its components. Furthermore aspects of data handling and computing are addressed.

3.1. Collider Physics

In high energy physics, the study of particle interactions plays an important role. Information about the initial particles as well as new particles (produced in collisions) can be gained through experiment. In fixed target experiments, particles are accelerated and directed at a matter target. As the target can consist of a great number of particles, it is possible to study processes with low rates of interaction. But due to momentum conservation only a small fraction of the initial beam energy is available for particle production, as the bulk of the energy has to account for the momentum of the new particles. Collider experiments use two beams of accelerated particles which are then brought to collision. The advantage of colliders with beams of the same energy is that the center of mass system can also be the lab frame, so the entire energy of the two beams can be used for particle production. A measure of the available energy is the center of mass energy $\sqrt{s}$. If the particles in both beams have the same mass and energy, then the center of mass energy is:

$$\sqrt{s} = 2E_{Beam}. \tag{3.1}$$

There are two main types of accelerators: Linear and circular. In both cases, charged particles are accelerated in electric fields. In linear colliders the distance of acceleration is only passed once, thus limiting the maximum beam energy. A cyclotron utilizes a constant $\vec{B}$-Field to force the particles on an outgoing spiral as they pass the accelerating $\vec{E}$-Field multiple times. Another circular accelerator is the synchrotron, in which the particles are held on an orbit of constant radius by varying the magnetic field according to the current particle energy.

The choice of particles to be collided depends among other things on the desired center of mass energy. Electrons have the advantage of being stable, which allows for

long storage times, and elementary, which leads to collisions with well known initial states. But their low mass ($m_e = 511\,\mathrm{keV}$) causes high energy loss per revolution through synchrotron radiation at relativistic speeds:

$$\Delta E \propto \frac{E^4}{R \cdot m_e^4}, \tag{3.2}$$

where R is the radius of the beam ring.

LEP[1] and LEP II, the predecessors of the LHC, have reached center of mass energies of about $\sqrt{s} = 200\,\mathrm{GeV}$. To reach higher energies heavier particles have to be collided. At the LHC protons are chosen. Unfortunately, there is a trade-off for the gain in energy: As protons have a substructure, the energy fraction of the interacting constituents is unknown. Parton distribution functions (PDF) are used to describe the probability to find a parton in the proton with a certain energy fraction x at a given resolution scale.

Another important quantity for colliders is the instantaneous luminosity $\mathcal{L}$ per bunch crossing:

$$\mathcal{L} = \frac{N_1 N_2 n_b f}{4\pi \sigma_x^* \sigma_y^*}. \tag{3.3}$$

It highly depends on properties of the beam. N_i stands for the number of particles in a single bunch in beam i, n_b is the number of bunches in the beam, f the revolution frequency, and σ_x^* and σ_y^* are the widths of the Gaussian beam profile at the interaction point in x and y direction. The luminosity is a measure for the expected event rate for a given process with the cross section σ:

$$\dot{N} = \sigma \mathcal{L}. \tag{3.4}$$

Integration over time then gives the total number of expected events depending on the cross section and the integrated luminosity $L = \int \mathcal{L} dt$.

3.2. Large Hadron Collider

The Large Hadron Collider (LHC) [18] is a proton-proton-collider at CERN[2] near Geneva, Switzerland. In the previous experiment LEP, electrons and positrons were brought to collision. Because of their opposite charges only one magnet system was required. Now, with protons going in both directions an additional beam pipe with

[1] Large Electron-Positron Collider
[2] Conseil Européen pour la Recherche Nucléaire

another magnet system (opposite magnetic dipole fields) had to be installed in the underground tunnel of 26.7 km circumference. There are 1232 main dipole magnets placed along the ring to deflect the beam with B-fields of up to 8.33 T (for the maximum beam energy of 7 TeV) and several thousand multipole magnets for focussing the beam. To account for the limited space both beam pipes share one cooling system, using liquid helium to cool the machine down to 1.9 K.

The properties of the beam are limiting the parameters in equation (3.3). The revolution frequency reaches up to $f \approx 1.1\,\text{GHz}$, limited by the maximum velocity of the protons in the beam approaching the speed of lightand the fixed tunnel radius. The number of protons per bunch depends on nonlinear beam-beam interactions as well as on the size of the beam pipe, which leads to a maximum of $N_i = 1.15 \times 10^{11}$ for a nominal bunch spacing of 25 ns. For a 50 ns bunch spacing higher N_i have been realized. The number of bunches per beam is $n_b = 2808$.

The LHC is designed to reach a center of mass energy of $\sqrt{s} = 14\,\text{TeV}$. There are four big experiments at different interaction points (IP) along the ring. ATLAS [19] and CMS (see section 3.3) are multipurpose detectors aiming for high luminosities up to $10^{34}\,\text{cm}^{-2}\text{s}^{-1}$ in proton collisions. LHCb [20] is specialized in studying B-physics at a lower luminosity. The detector is a single-arm forward spectrometer. ALICE [21] is designed for lead ion collisions, which can also be performed at the LHC with a peak luminosity of $10^{27}\,\text{cm}^{-2}\text{s}^{-1}$.

3.3. Compact Muon Solenoid

Located at Point 5 on the French side of the CERN area, the Compact Muon Solenoid (CMS) detector [22] is one of four main experiments at the LHC. It is designed as a high luminosity multipurpose detector. In fig. 3.1 a perspective view is shown, displaying the general layout. The detector is 21.6 m in length, 14.6 m in diameter and weighs a total of 12 500 t. A cylindrical layout is chosen to cover a wide detection range for particles going in all directions while leaving space for integrating the beam pipe. The barrel region is composed of 5 wheels and there is an endcap on either side. The main components are the inner tracker, directly surrounding the interaction point, followed by the calorimetry, consisting of an electromagnetic and a hadronic calorimeter. Positioned around this is the superconducting (eponymous) solenoid for bending the tracks of the charged particles. It is designed to generate a B-field of up to 4 T. On the outside the layers of the muon system are integrated into the iron return yoke of the solenoid. Therefore, muon tracks are bent twice in different directions inside and outside of the magnet coil, allowing for very good measurement of the muon charge and momentum. A more detailed description of the different

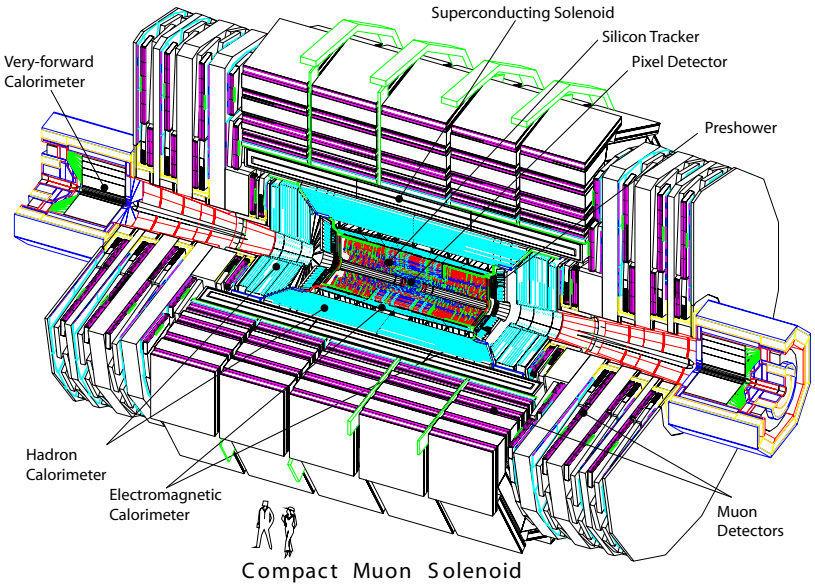

Figure 3.1.: The CMS detector in a perspective view [22]

elements of the CMS detector can be found in the following sections.

For a consistent description of particle trajectories in different coordinate systems, CMS uses a convention for the Cartesian coordinates. As origin the nominal interaction point is chosen, the x-axis points radially inward towards the center of the storage ring, the y-axis straight up and the z-axis in direction of the beams. The positive z direction is set to point along the ring counter clockwise (viewed from above), thus defining a right handed coordinate system. In polar coordinates, the azimuthal angle ϕ is then measured from the x-axis in the x-y-plane, in which the radial component r is also given. The polar angle θ is measured from the z-axis. Because θ is dependent on boosts in z-direction, it is convenient to define the pseudorapidity η:

$$\eta = -\ln\left(\tan\left(\frac{\theta}{2}\right)\right), \tag{3.5}$$

which is a good approximation for the rapidity y for relativistic particles. The advantage of this definition is that the difference in rapidity of two particles $\Delta y = y_1 - y_2$ is invariant under Lorentz-boosts making it possible to compare the distances of particles in events with different boosts.

3.3.1. Inner Tracker

A cylindrical volume of 2.6 m diameter and 5.8 m length along the beam direction contains the different layers of the inner tracker. The purpose of the tracker is the momentum measurement as well as a precise determination of the position of primary and secondary vertices in both the ϕ-r-plane and the z-direction. This is important for the identification of heavy flavours. There are 3 layers of silicon pixel detectors near the interaction point for high precision measurements of the impact parameter and the position of secondary vertices. 10 additional layers of silicon microstrip detectors surround the pixel tracker. Being located so close to the collision point, the tracker has to be able to handle hits from about 1000 particles per bunch crossing. This requires a high granularity and a fast response as well as high radiation hardness. Cooling the tracker is also important to minimize the radiation damage. It operates at $-10\,^{\circ}\mathrm{C}$.

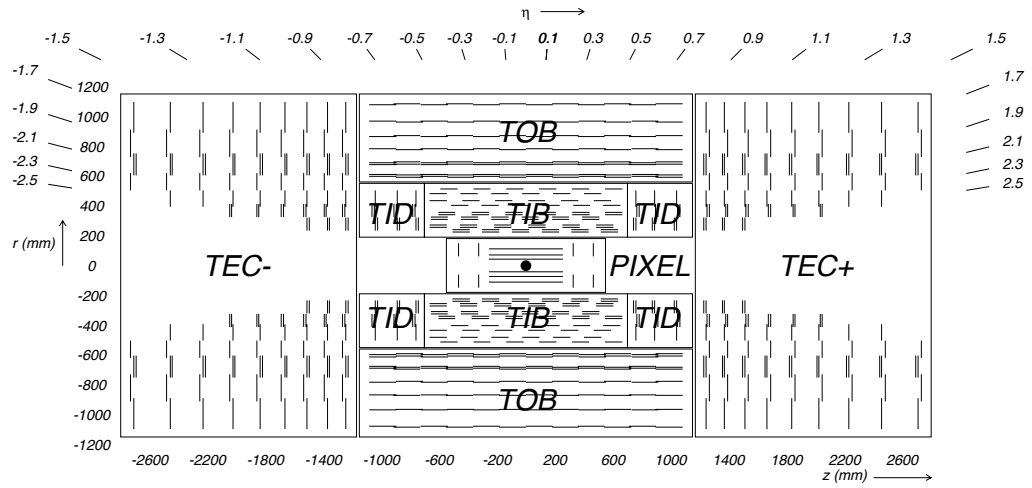

Figure 3.2.: Schematic of the inner tracker. The lines represent the alignment of the tracker modules. Double lines denote double sided modules [22].

- **Pixel Tracker**

  Three 53 cm long barrel layers are located at radial distances of 4.4, 7.3 and 10.2 cm. Together with two endcap disks (inner radius: 6 cm, outer radius: 15 cm) on either side placed at $z = \pm 34.5\,\mathrm{cm}$ and $z = \pm 46.5\,\mathrm{cm}$, the pixel detector covers a range of $|\eta| < 2.5$ in pseudorapidity. This arrangement of 66 million pixels (covering an area of $\sim 1\,\mathrm{m}^2$) allows for measuring of 3 tracking points in almost the entire pseudorapidity range. The size of a single pixel cell

is $150 \times 100\,\mu m^2$ (in z-direction and ϕ-r). Due to the magnetic field there is an electron drift in the pixels spreading the charge over more than one pixel. Analog readout of the pulse height allows for charge interpolation leading to a resolution of $15 - 20\,\mu m$.

- **Silicon Strip Tracker**

  As the area to be covered by tracker modules obviously increases with the distance to the interaction point, silicon micro-strip modules are used. These reduce the number of required read-out channels at the cost of measuring only one coordinate with high resolution, either z or ϕ. To account for that some modules are double sided with the strips on one side perpendicular to those on the other side. 29 different module designs of silicon strip trackers are installed around the pixel tracker. The Tracker Inner Barrel (TIB) consists of four layers at radii from 25.5 to 49.8 cm (see fig. 3.2). The two innermost are double sided modules, while the other two are single sided modules. On each side of the TIB three identical Tracker Inner Disks (TID) are placed between $z = \pm 80$ cm and $z = \pm 90$ cm. Each TID is built from three rings with radii from 20 to 50 cm. The outer one consists of single sided modules, the inner two of back-to-back modules. The Tracker Outer Barrel (TOB) has six layers surrounding TIB and TID (radii: 60 to 108 cm). As in the TIB the two innermost layers have double sided modules. The Tracker End Caps (TEC) add another nine tracker layers (placed between $z = \pm 1.24$ and $z = \pm 2.8$ m on either side) in the forward directions.

For high p_T tracks, the transverse impact parameter resolution reaches $10\,\mu$ m. The resolution of the first pixel hit is essential. At lower track momenta the resolution decreases due to multiple scattering. The momentum resolution of the inner tracker is [23]:

$$\frac{\delta p_T}{p_T} = \sqrt{(c(\eta) \cdot p_T)^2 + (0.5\,\%)^2}, \tag{3.6}$$

with p_T given in TeV and $c(\eta) = 15\,\%$ for $|\eta| \leq 1.6$ increasing to $c(\eta) = 60\,\%$ for $|\eta| = 2.5$.

3.3.2. Electromagnetic Calorimeter (ECAL)

Calorimeters are used to destructively measure the energy of a particle. In the ECAL, mainly particles which interact electromagnetically are absorbed. Those are electrons and photons. Muons only loose a fraction of their energy and have to be handled separately. The CMS ECAL consists of 61 200 lead tungstate ($PbWO_4$) crystals in the barrel region and 7324 in each endcap. As the compact design only leaves limited

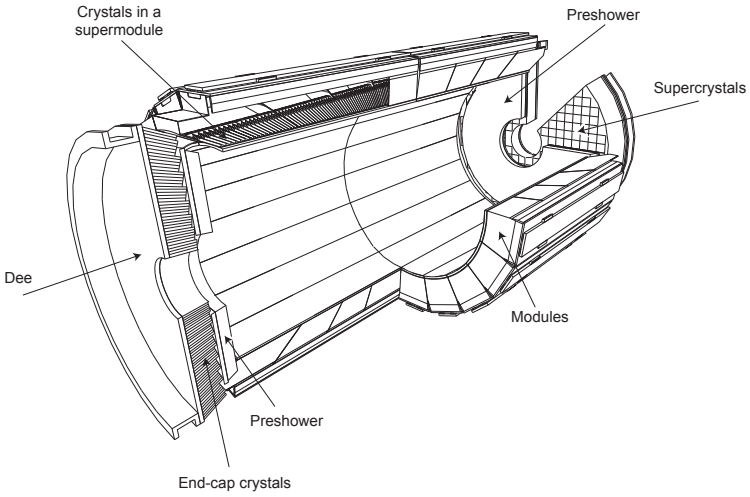

Figure 3.3.: Layout of the CMS electromagnetic calorimeter [22].

space for the calorimeter, lead tungstate with its high density ($8.28\,\mathrm{g\,cm^{-3}}$) and short radiation length ($X_0 = 0.89\,\mathrm{cm}$) is an ideal material. The barrel crystals are tapered with a cross section of $22 \times 22\,\mathrm{mm^2}$ on the inside and $26 \times 26\,\mathrm{mm^2}$ on the outside. Their length is 230 mm ($25.8\,\mathrm{X_0}$). In the endcaps, the crystals have a slightly bigger cross section (up to $30 \times 30\,\mathrm{mm^2}$) and are 10 mm shorter. The used photodetectors for the readout are avalanche photodiodes (APDs) in the barrel and vacuum phototriodes (VPTs) in the endcaps. In front of each ECAL endcap (EE), a preshower detector is placed (see fig. 3.3). The purpose of this sampling calorimeter is to identify neutral pions decaying into two photons, which otherwise would be measured as one high energy photon in the ECAL. The energy resolution of the ECAL, when summing 3×3 crystals, has been measured to be [22]:

$$\frac{\delta E}{E} = \sqrt{\left(\frac{2.8\%}{\sqrt{E}}\right)^2 + \left(\frac{0.12}{E}\right)^2 + (0.30\%)^2}, \tag{3.7}$$

where E is given in GeV. The different contributions are the stochastic, a noise and a constant term.

3.3.3. Hadronic Calorimeter (HCAL)

Hadronic jets from the strong interaction are only partially absorbed in the ECAL, therefore another calorimeter is needed. The main parts of the hadronic calorimeter -

hadronic barrel (HB) and hadron endcaps (HE) - are located between the ECAL and the magnet coil (barrel radius 1.77 to 2.95 m). Additionally two forward calorimeters (HF) are positioned at $z = \pm 11.2\,\mathrm{m}$, which cover the pseudorapidity range from $|\eta| = 3$ to $|\eta| = 5$ (as shown in fig. 3.4). The HB and HE sampling calorimeters are each built from 36 wedges consisting of over 30 alternating layers of absorber (steel and C26000 cartridge brass) and scintillator material (Bicron BC408 and Kuraray SCSN81). The granularity for $|\eta| < 1.6$ is $\Delta\eta \times \Delta\phi = 0.087 \times 0.087$. Since the space inside the solenoid is very limited, the absorption in EB and HB together is not sufficient for hadron showers in the low $|\eta|$ region. As a tail catcher for $|\eta| < 1.3$ the hadron outer (HO) is placed outside of the magnet. The coil itself functions as an absorber and a scintillator layer is put between the iron return yoke and the first layer of the muon barrel for each of the five barrel wheels. The middle one, having the shortest absorption depth, has an additional scintillator layer on the inside of the yoke. The energy resolution of the HCAL is:

$$\frac{\delta E}{E} = \sqrt{(frac120\,\%\sqrt{E})^2 + (6.8\,\%)^2}, \tag{3.8}$$

where E is given in GeV.

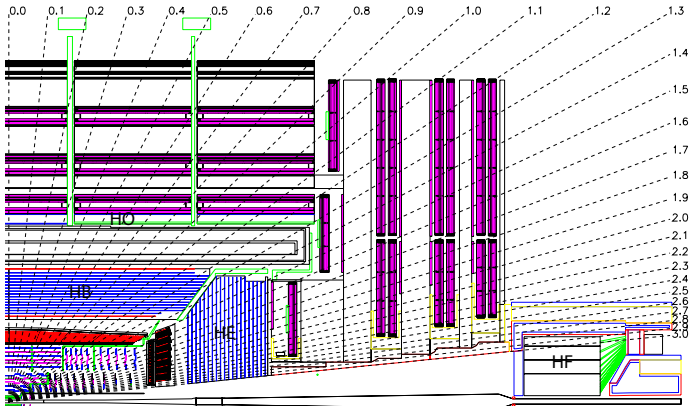

Figure 3.4.: Longitudinal view of the CMS hadronic calorimeter [22].

3.3.4. Solenoid

The superconducting coil is able to generate a magnetic field of up to 4 T (operating at 3.8 T) for bending the tracks of charged particles in the detector. It measures 12.5 m in length, 6.3 m in diameter and weighs 220 t. The 4-layer winding is made from NbTi

and it can store 2.6 GJ of energy at full current. For returning the flux a 10 000 t iron yoke is placed around the solenoid. The yoke consists of five barrel wheels and three endcap disks on either side. To become superconducting the magnet has to be cooled down to about $T_g = 6.4\,\mathrm{K}$. The operating temperature of 4.5 K leaves a margin of 1.9 K.

3.3.5. Muon System

Precise muon measurement plays an important role in many interesting processes (e.g. the Standard Model Higgs decay $H \to ZZ \to 4\mu$ or the decay $Z \to 2\mu$ in this analysis), as muons are less prone to radiative loss in the tracker than electrons, and therefore reach the muon system less biased. The CMS muon system is designed for muon identification, measurement of their momentum as well as triggering on muon events. Three different types of particle detectors are used. In the barrel region ($|\eta| < 1.2$) a combination of drift tube (DT) chambers and resistive plate chambers (RPC) are arranged in four stations in between the iron yoke. Each station consists of 12 DT chambers: two sets of 4 for the measurement in the r-ϕ-plane and 4 for the z-direction. The fourth station has no chambers for the z-direction. The RPCs have a fast response and good time resolution, which is ideal for triggering. Two layers are built into each of the two inner stations and one layer each in station 3 and 4. This way low p_t muons, that do not reach the outer stations, can still be triggered. Because of the high muon rates, high background level, and non-uniform magnetic field in the endcaps, cathode strip chambers (CSC) are used instead of drift tubes. They are also subdivided into four stations and cover a pseudorapidity range of 0.9 to 2.4. The first three stations also contain RPCs. In fig. 3.5, the layout of the different chambers can be seen.

3.3.6. Trigger System

With the high bunch crossing frequency of 20 MHz and the high number of collisions at each crossing (up to 40) for pp-collisions, it is impossible to store the data of each and every event. Therefore, an efficient way to preselect interesting events has to be implemented. CMS uses a two step trigger system: Level-1 Trigger (L1) and High-Level Trigger (HLT). The former one is an online trigger of programmable hardware. Coarse data from the calorimeters and the muon system are evaluated to decide whether to store the precise data of an event for the HLT triggering step. The latency of the L1 is 3.2 µs. During this interval, the processing is pipelined to avoid dead-times. The HLT is a software trigger performing calculations similar to those in

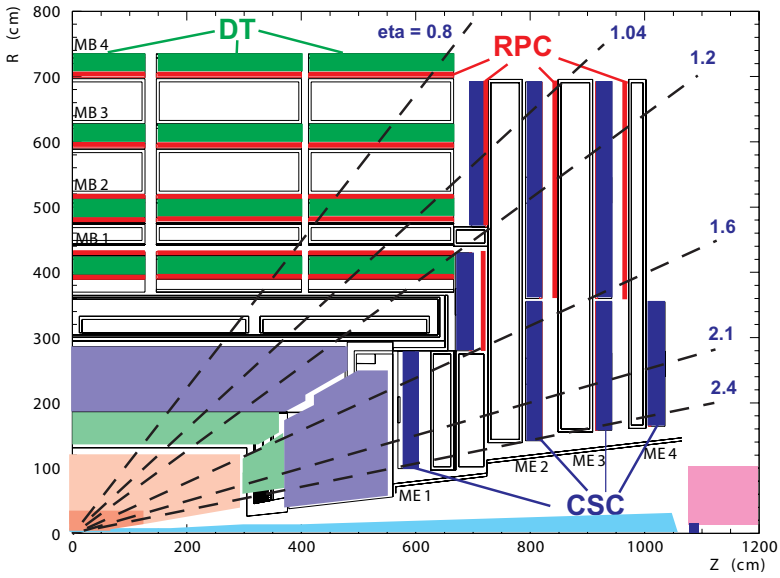

Figure 3.5.: Layout of the muon system showing the arrangement of DT, CSC and RPC [24].

the subsequent offline particle reconstruction of the triggered data. The output rate of the L1 is 30 kHz. Combined with the HLT triggering the designed reduction of the output rate is a factor of at least 10^5.

3.3.7. Luminosity Measurement

As stated in sec. 3.1, the luminosity plays an important role in collider experiments as it gives information about the beam quality and at the same time is key to the calculation of event rates. Therefore, high precision methods for luminosity measurements are needed. The idea is to measure the rate R of events with the visible cross section σ_{vis} of the considered process (e.g. lepton pair production from double photon exchange). Formula 3.4 then gives the luminosity. Two different parts of the detector can be utilized for that purpose [25]. The Hadron Forward Calorimeter (HF) is capable of on-line measurements as it can handle unstable beams. Due to detector effects causing calibration drift, this HF based luminosity loses in accuracy over the long run. The handling of pile-up also complicates good measurements. In contrast, luminosity measurements in the pixel detector prove to be very precise, but require a stable beam and can only be performed offline. In the pixel cluster counting method, zero-bias events are used. They only require two bunches crossing the interaction

point to be triggered. The per-bunch luminosity L is proportional to the number of collisions per crossing μ:

$$\nu\mu = L\sigma_T, \tag{3.9}$$

where ν is the revolution frequency of the bunches and σ_T the total inelastic cross section. The average number of clusters per event $\langle n \rangle$ in the pixel detector is the product of the average number of clusters per collision n_1 and μ. With $\sigma_{vis} = \sigma_T n_1$ the luminosity is:

$$L = \frac{\nu\langle n \rangle}{\sigma_{vis}}. \tag{3.10}$$

To calibrate the measurements dedicated Van der Meer Scans are used to determine σ_{vis} by measuring L using the beam properties and $\langle n \rangle$ at the same time.

3.4. Computing Environment

3.4.1. Grid

The Worldwide LHC Computing Grid (WLCG) [26] provides the computing power and infrastructure for handling the huge amount of data (about 25 Petabyte per annum) generated at the LHC. Computing centres in almost 40 countries around the world are linked to the network. The grid is organized in a Tier system. Tier-0 is the CERN Computing Centre. Its main purpose is the safe-keeping of the raw data and first pass reconstruction and their distribution to Tier-1s, but it also provides computing capacity. Next there are 12 Tier-1s, large computing centres responsible for the reconstruction and storage of raw data as well as the reconstruction output. Additionally they handle simulated event production. Tier-2s are smaller computing facilities typically located at institutes or universities where copies of the data samples are stored and which are accessible for all scientists involved. Small local clusters or even single computers, connected to the grid, are sometimes referred to as Tier-3s.

3.4.2. CMSSW

To standardize the common tasks in the handling of the data, the CMS collaboration has developed a modular software framework called CMSSW [27]. In its Event Data Model (EDM), all raw and reconstructed data that originate from a single physical collision are stored as an Event. All contained objects can be accessed and stored in ROOT files. So, it is possible to use ROOT [28], a high energy physics software

tool developed at CERN. CMSSW provides implementations for reconstruction, simulation, calibration and alignment and can handle real and MC simulated data alike. Several output formats are provided. For MC simulation the full information after generation and detector simulation can be stored as GEN-SIM. The reconstructed data is saved in the RECO format or further optimized for analysis as Analysis Object Data (AOD).

3.4.3. ACSusyAna

In this thesis, the software framework ACSusyAna [29], developed at the III. Physikalisches Institut A, is used for the analysis. In the first step AOD data samples are skimmed using the grid: very basic selection cuts (i.e. on the transverse momenta p_T of muons or jets) are applied to reduce the amount of data; the output is stored as flat ROOT n-tuples. Those are then locally reskimmed with more analysis specific cuts before the analysis code, containing the selections and cuts described in sections 5.4 and 5.5, is run.

4. Object Reconstruction

In order to achieve meaningful results, a good reconstruction of the physics objects is necessary. The detector data (real, or simulated) has to be interpreted accurately to identify the object that caused the detector response. Track reconstruction is part of the identification, but also enables a precise energy measurement of the object. In the following, the methods for reconstruction of the different objects crucial to the analysis are described.

4.1. Particle Flow Algorithm

The Particle Flow (PF) algorithm [30] takes all available detector information into account when calculating the object properties in the event. All stable particles like muons, electrons, and photons, and charged and neutral hadrons are determined by combining all CMS sub-detectors. Jets (see 4.4) are then built using the already identified particles in the event. Subsequently, the missing transverse energy is calculated from the transverse momenta of the jets and the remaining particles. So, it depends on the measurement of every other object in the event. Here, PF reconstruction is applied to the muons, jets and missing transverse energy.

4.2. Muons

Muons lose just a very small amount of energy in the calorimetry and are the only visible particles that reach the muon system of CMS. This also means their tracks are bend twice in the 3.8 T magnetic field of the solenoid, leading to momentum measurements of high precision.

For the start of the track reconstruction in the pixel detector, any two hits consistent with a track could be chosen. But the algorithm for finding pairs [31] starts by selecting an outer hit and searching for another hit in between this first hit and a known vertex or the beam spot. The resulting pair of inner and outer hit (each on a different tracker layer) defines the seed for the pattern recognition in the tracker. The

track building uses a Kalman filter [32] (linear fitting algorithm). Based on all the hits already associated with the track, the algorithm predicts the location of the next hit which significantly reduces the size of the search region. When the appropriate hit is found, it is added to the track. Through iteration, the complete track is built from the center outwards. This method also works for tracks in the muon system, where there are much less hits, but almost exclusively from muons.

Depending on the reconstruction the muon is categorized as:

- standalone muon
  If the track is only reconstructed in the muon system, the muon is considered standalone. However due to the high tracker efficiency only about 1 % of the muons reach the muon system without being detected in the tracker.
- tracker muon
  Tracker muons are reconstructed in the tracker, which gives a better momentum resolution than the muon system. To be counted the extrapolation of the track must match at least one hit in a muon chamber segment.
- global muon
  The combination of a track in the muon system matched to a tracker muon gives the best possible muon measurement, as the tracker information improves the resolution.

4.3. Electrons

Electrons are best identified in the ECAL as they are unique in causing superclusters there. Photons and electrons usually deposit most of their energy in a 5×5 crystal cluster, but as electrons are bend by the magnetic field they emit bremsstrahlung, expanding the region of energy disposition. The search [33] for a seed in the pixel tracker is therefore constraint to a region between such a supercluster and the beamspot consistent with a possible electron track. After the seed is chosen, a track building method very similar to that of the muons is applied. Instead of a Kalman filter which estimates the energy loss by using a single Gaussian distribution, a Gaussian sum filter [34] is used. It models the bremsstrahlung energy loss distribution by a mixture of several Gaussians thus improving the electron momentum resolution.

4.4. Jets

A cascade of hadrons shows a characteristic signal in the detector referred to as jet. Single quarks or gluons produced in an event are the starting points of hadronization. The quark immediately forms a hadron with other quarks as it needs to be in a bound state (except for the top quark which decays into a bottom quark first). In the following decay process, more hadrons are produced due to the color confinement, because the energy of the gluon field between detaching quarks increases. All of the particles in a jet have a momentum direction similar to the original particle. In order to identify it and calculate its momentum, the constituents of the jet are combined using sequential jet clustering algorithms. The CMS group supports SISCone, k_t and anti-k_t. The latter [35] is used in this analysis. The principle is to define two distances: d_{ij} between particle i and particle or pseudojets j and d_{iB} between i and the beam B. In the clustering process, the distances are compared for every single particle i. If d_{ij} is smaller i and j are recombined into a pseudojet, while if d_{iB} is the smaller one i is called a jet and removed from the list of particles. This is repeated until all remaining particles are associated to a jet. The resulting jets are cone-shaped, infrared and collinear safe. A cone size of $R = 0.5$ is used in the definition of d_{ij}.

4.5. Missing Transverse Energy

Although the detector has a high pseudorapidity coverage, particles moving in a very forward direction may not be measured as they leave the detector through the area of the beam pipe. Their momentum would be lost, but the loss in transverse momentum would only be very small. This leads to higher precision measurements in the transverse plane. A significant imbalance in the sum of the transverse momenta of all detected particles indicates that something left the detector without leaving a signal. In the Standard Model, only neutrinos escape detection. Missing transverse energy can therefore be used in the search for new physics that predict undetectable new particles, as long as no neutrinos are involved in the signal.

The reconstruction of E_T^{miss} in its simplest form [36] is building the negative vectorial sum over all uncorrected energy deposits in projective calorimeter towers. In this analysis, PF MET [30] is used instead. It is calculated from the transverse momenta of the already reconstructed particles and jets in the event which is referred to as clustered energy and previously unassigned, unclustered energy. Several types of corrections can be applied or propagated respectively:

- Type-0:

Corrects for estimates of neutral pile-up contributions as well as identified charged pile-up contributions

- Type-1:
  Corrections on the jet energy scale applied by adding an offset to the jets before calculating the PF MET
- Type-2:
  Additional corrections on the unclustered energy (Not recommended for PF MET)

The Type-1 correction is used in the current work.

5. Analysis

In this chapter the different aspects of the analysis are presented. Starting with a description of the used data, including the production of the Monte Carlo backgrounds and the signal samples. Next, following the order in the analysis, the object and event selection are described. Then the cuts for background reduction are presented. Finally all the applied corrections and calculated systematic uncertainties are described.

5.1. Background MC Samples

To compare the data taken by the CMS experiment with predicted signals of a new theory, a good simulation of the Standard Model background is important. Especially outside of the signal region the different background processes should give a precise description of the data. For the generation of Standard Model background samples a variety of Monte Carlo generators can be utilized. The samples used in this analysis are produced with the multi-purpose generator PYTHIA6[37]. With the high number of particles in the final state of a real event, simulation is not trivial and has to be broken down into smaller steps. First, the hard interaction of the two initial particles (or partons) is simulated producing only a few "final state" partons, which would then branch or decay. Beside multi-purpose generators special Matrix Element (ME) generators (such as POWHEG[38] or MADGRAPH[39]) can calculate this parton-level information, which is then used as input for the next steps, where the decay and hadronization of the partons is simulated according to theoretical probabilities. Finally, the detector response to the fully hadronized events has to be simulated, as the real data is reconstructed from measurements in the detector. The CMS detector simulation is done in GEANT4[40], a toolkit for simulating the passage of particles through matter. Additionally, to account for pile-up (see section 5.7.1), the simulated events are mixed with a minimum bias dataset.

Standard Model processes that have a similar signature as the signal process Z + $\mathcal{U}$ are Drell-Yan (DY), Diboson production and $t\bar{t}$ generation. DY is special as the process $Z/\gamma* \rightarrow l\bar{l}$ itself does not account for missing transverse energy (MET), which instead is due to detector effects and pile-up. Still DY is the dominant background

at low MET, because of its high cross section. In all the other background processes, neutrinos are produced, which then escape the detector undetected and add to the MET. Initially, also WJets and QCD processes were considered for their even higher cross sections (37.5 nb and 134.7 nb respectively), but did not contribute significantly as their signatures differ too much from the signal.

A summary of the background samples in this analysis can be found in table 5.1. All of them are produced with the tune Z2* (a set of optimised parameter settings for the MC generator) and use the CMS Standard PDF set CTEQ6L. An exception are the three TT ($t\bar{t}$) samples, that use CT10. Those are also binned in the invariant mass of the top pair to gain some statistics in the high MET tail. For additional comments on the cross section uncertainties see section 5.7.8.

5.2. Signal MC Samples

For the signal samples in LO, PYTHIA8[43] is used, since unparticles are part of its implementation [44]. The process $f\bar{f} \to \mathcal{U}Z$ is provided as part of the Extra Dimensions production routines. The most important parameters that can be specified are $d_\mathcal{U}$, $\Lambda_\mathcal{U}$, λ, unparticle spin, minimum Z mass (50 GeV), and desired Z decay products (muons).

Only integral spins $[0, 1, 2]$ are supported. Here, spin 0 is chosen as it has the highest cross section and therefore the best chances for discovery. The unparticle dimension is restricted by theory. For spin 0, it can not be ≤ 1 due to the conformal invariance (see also 2.2.2). The upper limit at $d_\mathcal{U} = 2$ is more of a soft limit, hence the chosen range is 1.01 to 2.2.

For the cut off parameter $\Lambda_\mathcal{U}$, a single arbitrary value of 15 TeV is used in the production. According to [9] the differential cross section is:

$$\frac{d^2\sigma}{dP_\mathcal{U}^2\,dt}(f\bar{f} \to Z + \mathcal{U}) = \frac{|\bar{\mathcal{M}}|^2}{16\pi \cdot s^2}\frac{A_{d_\mathcal{U}}}{2\pi\Lambda_\mathcal{U}^2}\left(\frac{P_\mathcal{U}^2}{\Lambda_\mathcal{U}^2}\right)^{d_\mathcal{U}-2}\theta(P_\mathcal{U}^0)\theta(P_\mathcal{U}^2) \tag{5.1}$$

$$\sim \Lambda_\mathcal{U}^{2-2d_\mathcal{U}} \tag{5.2}$$

where $P_\mathcal{U}$ is the invariant mass of the unparticle, $|\bar{\mathcal{M}}|$ is the matrix element, s the Mandelstam variable and $A_{d_\mathcal{U}}$ is a normalisation constant related to the unparticle phase space. The Heavyside functions $\theta(P_\mathcal{U}^0)$ and $\theta(P_\mathcal{U}^2)$ ensure a positive energy and unparticle mass. For a given $d_\mathcal{U}$ the cross section only depends on $\Lambda_\mathcal{U}$. This means that samples for different cut off parameters can be derived by scaling the cross section of the 15 TeV samples accordingly.

process	sample name	# gen. events	σ/pb	$\Delta\sigma$ / pb	σ order
$Z/\gamma* \to ll$	DYJetsToLL_M-50_$\diamond$-madgraph-tarball/$\triangleright$-v1	30459503	3503.71	$\pm 5\,\%^{\star}$	NNLO
$t\bar{t}$	TT_CT10_$\diamond$-powheg-tauola/$\triangleright$-v2	21675970	245.8	$+2.5\,\%, -3.4\,\%$	NNLO
$t\bar{t}$	TT_Mtt-700to1000_CT10_$\diamond$-powheg-tauola/$\triangleright$-v1	3082812	245.8	$+2.5\,\%, -3.4\,\%$	NNLO
$t\bar{t}$	TT_Mtt-1000toInf_CT10_$\diamond$-powheg-tauola/$\triangleright$-v1	1249111	245.8	$+2.5\,\%, -3.4\,\%$	NNLO
$t \to bl\nu$(tW-channel)	T_tW-channel-DR_$\diamond$-powheg-tauola/$\triangleright$-v1	497658	11.1	± 0.3	approx. NNLO
$t \to bl\nu$ (t-channel)	T_t-channel_$\diamond$-powheg-tauola/$\triangleright$-v3	99876	56.4	$+2.1, -0.3$	approx. NNLO
$t \to bl\nu$ (s-channel)	T_s-channel_$\diamond$-powheg-tauola/$\triangleright$-v1	259961	3.79	± 0.07	approx. NNLO
$\bar{t} \to bl\nu$(tW-channel)	Tbar_tW-channel-DR_$\diamond$-powheg-tauola/$\triangleright$-v1	493460	11.1	± 0.3	approx. NNLO
$\bar{t} \to bl\nu$ (t-channel)	Tbar_t-channel_$\diamond$-powheg-tauola/$\triangleright$-v1	1935072	30.7	± 0.7	approx. NNLO
$\bar{t} \to bl\nu$ (s-channel)	Tbar_s-channel_$\diamond$-powheg-tauola/$\triangleright$-v1	139974	1.76	± 0.01	approx. NNLO
$ZZ \to ll\nu\nu$	ZZJetsTo2L2Nu_$\diamond$-madgraph-tauola/$\triangleright$-v3	954911	0.33	$\pm 3\,\%^{\star}$	NLO
$WW \to l\nu l\nu$	WWJetsTo2L2Nu_$\diamond$-madgraph-tauola/$\triangleright$-v1	1933235	5.76	$\pm 4\,\%^{\star}$	NLO
WZ	WZ_$\diamond$_pythia6_tauola/$\triangleright$-v1	10000283	33.21	$\pm 4\,\%^{\star}$	NLO

Table 5.1.: List of background samples in the analysis in AODSIM format. POWHEG samples are produced in NLO, the others in LO. Cross sections for the given order are taken from [41]. *: uncertainties estimated from values in [42], $\diamond$: TuneZ2star_8TeV, $\triangleright$: Summer12_DR53X-PU_S10_START53_V7A.

The coupling constant λ is not determined theoretically and could possibly vary for whether a fermion or a boson is interacting with the unparticle. For simplicity, λ is assumed to be 1 for all particles.

The officially produced signal samples are listed in table 5.2. The Standard tune in Pythia8 is 4C. The used PDF set is CTEQ6L.

$d_{\mathcal{U}}$	# events	σ/pb
1.01	50000	15.52
1.02	50000	25.52
1.04	50000	35.19
1.06	50000	36.97
1.09	50000	31.1
1.10	50000	29.2
1.20	50000	9.201
1.30	50000	2.435
1.40	50000	0.604
1.50	50000	0.14
1.60	50000	0.037 58
1.70	50000	0.008 583
1.80	50000	0.002 236
1.90	50000	5.01×10^{-4}
2.00	50000	1.43×10^{-4}
2.20	50000	1.04×10^{-5}

Table 5.2.: Unparticle signal samples and their production cross section. The full sample name for e.g. $d_{\mathcal{U}} = 1.6$ is Unpart_ZToMuMu_SU-0_dU-1p60_LU-15_Tune4C_8TeV-pythia8/Summer12_DR53X-PU_S10_START53_V7A-v1/AODSIM.

5.3. Dataset 2012

The full dataset of the four run periods performed in 2012 at $\sqrt{s} = 8\,\text{TeV}$ is used in this analysis. Over $20\,\text{fb}^{-1}$ of integrated luminosity were recorded between April and December 2012, of which $19.7\,\text{fb}^{-1}$ are certified.

As the data is better understood over time, new corrections and calibrations can be implemented. This process of refining the reconstruction enhances the data quality. The samples used here (see table 5.3) are from the latest re-reconstructions executed in

January 2013. The DoubleMu data stream is chosen, because it contains the relevant events with two muons.

run	sample name	run range
A	DoubleMu/Run2012A-22Jan2013-v1/AOD	190456 - 193621
B	DoubleMuParked/Run2012B-22Jan2013-v1/AOD	193834 - 196531
C	DoubleMuParked/Run2012C-22Jan2013-v1/AOD	198022 - 203742
D	DoubleMuParked/Run2012D-22Jan2013-v1/AOD	203777 - 208686

Table 5.3.: The full 2012 dataset for the analysis.

5.4. Object Selection

The aim of the object selection is to pick only well identified and well measured objects, which ultimately enhances the quality of the event selection and identification of the underlying process, thus helping in the separation of signal from background.

5.4.1. Muons

The selection criteria for muons concern their track reconstruction in the tracker and the muon system. CMS recommends different muon IDs [45], which are collections of quality cuts. In this analysis, the tight muon ID is applied to select the muons later used in the event selection. Apart from reconstruction as a global Particle Flow (PF) muon (see sec. 4.2), the following conditions have to be met:

- Distance from primary vertex: In the inner tracker the distance of the primary vertex and the impact parameter should be small: transverse distance $d_{xy} < 2\,\text{mm}$ and longitudinal distance $d_z < 5\,\text{mm}$
- Pixel hits: at least 1 pixel hit (important for a good track fit)
- Tracker layers: at least 5 tracker layers hit
- Track fit: $\frac{\chi^2}{N_{dof}} < 10$ is the required quality of the track fit in the inner tracker
- Muon chambers: at least one hit in a muon chamber should be used in the track fit
- Muon segments: segments in at least two muon stations should be hit (enabling a meaningful p_T measurement of the muon)

These cuts are made to suppress hadronic punch-through (causing a detector response in the first muon station), muons from decay in flight (only partially or not at all measured in the tracker) or even cosmic muons, and also ensure a good fit of the track.

The loose muon ID is chosen to veto on additional muons in an event. It just requires the muon to be a PF muon and to have hits in the tracker associated to it (tracker muon or global muon).

For the relative tracker-isolation of the muon, a PF based algorithm with $\Delta\beta$-correction for a cone size of $\Delta R = 0.4$ is applied:

$$\left(\sum_{CH} p_T + max[0., \sum_{NH} p_T + \sum_{\gamma} p_t - 0.5 \sum_{PU} p_T]\right) / p_T^{\mu} < 0.12 \tag{5.3}$$

with the sums of the transverse momenta of the PF objects except the muon candidate (charged (CH) and neutral hadrons (NH), photons (γ) and pile-up (PU)), that along with the muon add to the p_T of the track. Of all the contributions to the track p_T the one of the muon should be by far the highest to count as well isolated.

As the considered decay channel is $Z \to \mu\mu$, events with exactly two (tight) muons are selected. Because the Z is electrically neutral they are required to have opposite charges. Another quality cut is made on the transverse momenta of the muons. The used HLT trigger (see 5.5.1) has a turn-on, so to be on the safe side the p_T of the first (second) muon has be greater than 32 GeV (17 GeV). Events with additional loose ID muons are vetoed.

5.4.2. Electrons

Similar to the muons, the electrons are selected on a cut based ID [46]. Several working points define cuts on the Gaussian sum filter reconstructed (see sec. 4.3) electrons measured in the tracker and the electronic calorimeter. Due to deficient instrumentation of the ECAL between barrel and the endcaps, not the entire η-range is covered, but is instead divided in barrel ($|\eta| < 1.442$) and endcap region ($1.566 < |\eta| < 2.5$) with different cut values shown in table 5.4. The difference between the pseudorapidity (angle ϕ) of the electron supercluster and of the direction of the extrapolated tracker track is given by $|\Delta\eta_{in}|$ ($|\Delta\phi_{in}|$). A measure for the energy distribution over a 5×5 ECAL cluster is calculated as $\sigma_{i\eta i\eta}$, where the energies of the single crystals in the cluster are added with weights according to their position in the cluster. The ratio of energy deposit in HCAL over ECAL should be small as electrons are supposed to be mainly absorbed in the ECAL. d_0 is the transverse and d_z the longitudinal distance

between the primary vertex and the impact parameter. $|1/E - 1/p|$ gives the difference between the energy E of the supercluster and the momentum of electron track. Finally, a good isolation PF Iso / p_T is required. It uses a cone size of $\Delta R = 0.3$.

	veto	
cut variable	barrel	endcap
$\|\Delta\eta_{in}\|$	0.007	0.01
$\|\Delta\phi_{in}\|$	0.8	0.7
$\sigma_{i\eta i\eta}$	0.01	0.03
HCAL/ECAL	0.15	-
d_0/cm	0.04	0.04
d_z/cm	0.2	0.2
$\|1/E - 1/p\|$	-	-
PF Iso / p_T	0.15	0.15

Table 5.4.: All cut values of the cut based electron ID are upper bounds. Only electrons with smaller values pass the selection.

The veto electron ID is used to reject two muon events that contain extra electrons, e.g. from WZ production with a leptonic W decay.

5.4.3. PFJets

While jets are not part of the actual signal process, they are still important for the calculation of E_T^{miss}. They are also used in distinguishing signal and background events via jet multiplicity and in the b-tagging. The loose PF jet ID [47] is applied to jets with $p_T > 30\,\text{GeV}$: The neutral hadron fraction and the neutral electromagnetic fraction both have to be smaller than 0.99 and the number of constituents greater than 1. This ensures the jet is not made up from a single neutral particle. In the pseudorapidity region of $|\eta| < 2.4$, additional conditions have to be met: the charged hadron fraction and the charged multiplicity need to be greater than 0 and the charged EM fraction smaller than 0.99.

5.4.4. Missing Transverse Energy

The missing transverse energy is the most important object in this analysis as the unparticle, if it exists, can not be detected and thus would only show up as imbalance in the momentum/energy measurement. Here the Particle Flow based MET with

Type-I correction is used. See sec. 4.5 for a more detailed description. No further cuts or selection criteria are applied.

5.5. Event Selection

5.5.1. Trigger

In the first step of the event selection, the firing of an appropriate HLT trigger (see 3.3.6) is required. As the event should contain two good muons, a DoubleMu trigger is chosen. For HLT_Mu22_TrMu8 the triggering muon has to have a $p_T \geq 22\,\text{GeV}$ and a maximum pseudorapidity of $|\eta| = 2.1$. The second muon requires a transverse momentum of $p_T \geq 8\,\text{GeV}$.

5.5.2. MET filters

Not all of the data taken by the CMS experiment is suitable for analysis when missing transverse energy is considered. Known issues like unusual noise in the HCAL or the firing of calibration lasers during data recording are taken into account by applying MET filters, that reject such events. A full list of those filters can be found at [48]. In total, about 0.85 % of data events are filtered before any other cuts are applied.

5.6. Cut Based Analysis

After the general object and event selection, further cuts are applied, that are designed to reduce background as much as possible while keeping a high number of signal events. In the following, these cuts on properties of the signal process, which differ from at least one background process, are described. The distribution with the most promising difference between signal and background is the E_T^{miss} distribution, and will therefore be used in the calculation of the exclusion limits.

5.6.1. Z mass

Since the signal process contains a Z decay, the invariant mass of the two leptons should match the mass of the Z Boson ($m_Z = 91.1876\,\text{GeV}$). To allow for uncertainties on the Z mass and for off shell Zs, a mass region around the Z peak of $m_Z - 20\,\text{GeV} < M_{inv} < m_Z + 20\,\text{GeV}$ is chosen. The distribution of the invariant mass is shown in

figure 5.1. Clearly the Drell-Yan background cannot be significantly reduced by this cut as it also features a Z decay. But processes without a Z (Top and WW) are reduced and especially events with higher M_{inv} are excluded.

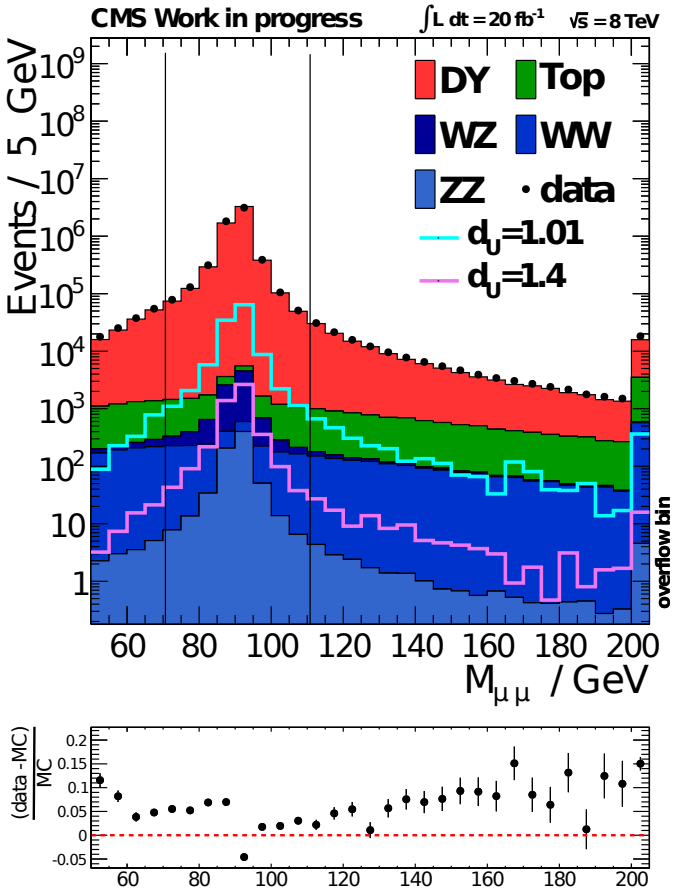

Figure 5.1.: Invariant mass of the two muons showing a peak at m_Z for background and signal. In addition to the dominant SM processes, two typical signal scenarios are shown. Uncertainties are statistical only.

5.6.2. Jet multiplicity

A cut on the number of selected PF jets can be used to reduce the contribution of background processes with actual jets in their signature. I.e. events with top decays should on average contain one jet (produced by b-quarks in the decay chain) for every top. So, for the $t\bar{t}$ background (dominant at higher MET) the number of jets peaks at 2 while the signal samples have their maximum at 0 jets (see fig. 5.2). Higher

jet multiplicities are the result of pile-up jets in the events or QCD radiation. To differentiate between signal and background the cut on the number of jets is set to $N_{jets} < 2$. A lower cut would significantly reduce the signal efficiency. A better approach is to further cut on b-tagged jets (see sec. 5.6.4).

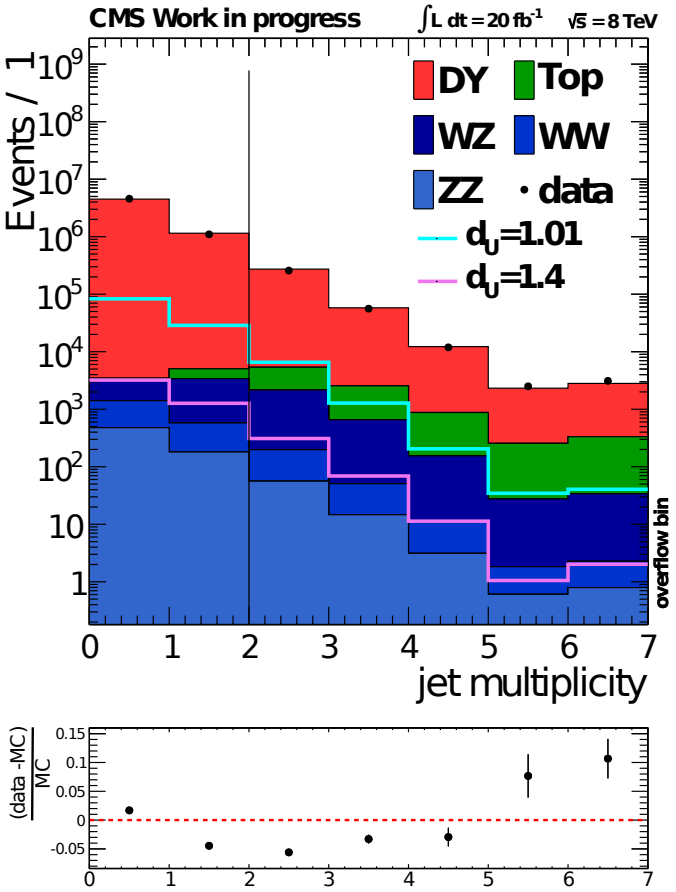

Figure 5.2.: Jet multiplicity after the Z mass cut. The top background peaks at 2 jets excluded by the cut on the number of jets ≤ 1.

5.6.3. Response of Z and MET

In the signal process initially only a Z boson and an unparticle are produced. Due to momentum conservation, their momenta should point, in leading order, in opposite directions ($\Delta\phi = \pi$) and have the same absolute value in the center of mass frame. Instead of only cutting on the difference in the angle ϕ, a cut on the response is intro-

duced, which combines angle and absolute value into one observable. The response u_{tot} is defined as:

$$\vec{u}_{tot} := -\vec{p}_T^{\,Z} - \vec{E}_t^{miss} \tag{5.4}$$

where the invisible unparticle is represented by the missing transverse energy and the transverse momentum of the Z is reconstructed from the two selected muons. The cut is applied to $u_{||}/p_T^Z$, where $\vec{u}_{||}$ is the component of $\vec{u}_{tot}$ that is parallel to $\vec{p}_T^{\,Z}$ (see fig. 5.3). For the signal samples, $u_{||}$ is close to 0 and the cut variable peaks at 0 accordingly, while processes with different relations of Z and MET show a shift to negative values. Especially in DY, where the MET is much smaller and its direction uncorrelated to the Z, $u_{||}/p_T^Z$ peaks at -1. Since the cut variable depends on the absolute value of the missing transverse energy, the cut optimisation (see 5.8) has to consider the cut on the MET itself. The chosen value is $u_{||}/p_T^Z > -0.3$. In fig. 5.4 the response distribution before the cut is shown.

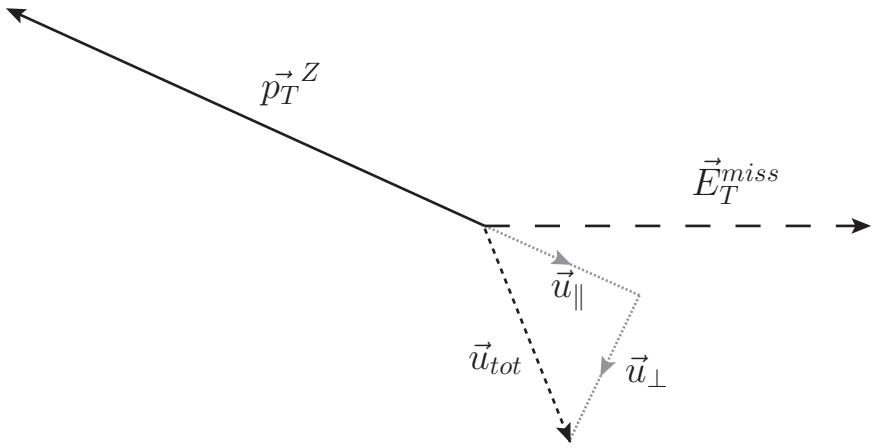

Figure 5.3.: Definition of the response of Z and MET.

5.6.4. B-tagging

A way to further reduce the number of events containing one jet is to check for b-tags. Especially the $t\bar{t}$ background has b-tagged jets as the top quarks decay into bottom quarks before hadronization. Several algorithms are implemented to determine whether or not a jet was produced by a decaying bottom quark. Each of these assigns a discriminator value to a single jet. This analysis uses the Combined Secondary Vertex (CSV) algorithm, as it is among the most efficient [49]. In addition

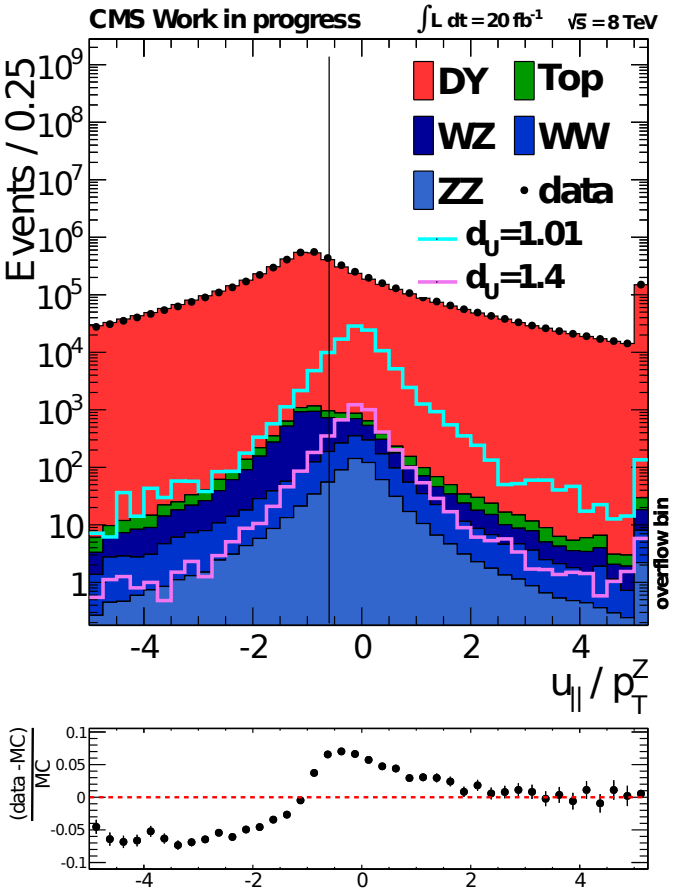

Figure 5.4.: Response after Z mass and Jet multiplicity cut. The uncertainties in the ratio plot are only statistical.

to the impact parameter significance, information about secondary vertices and jet kinematics are included in the calculation. The tight working point is chosen for its low misidentification probability of less than 0.1 %. The cut on the b-tag discriminator for CSV tight is at 0.898. Jets with values above are considered b-tagged and the cut on the number of those jets is $N_{bJets} < 1$.

5.6.5. MET

Because the missing transverse energy itself is the distribution used in the limit calculation, the cut on the MET is optimised (see sec. 5.8) in the process to find the best expected limit. The cut value varies over the range of the $d_{\mathcal{U}}$ signal samples, but

always lies above 100 GeV, thus effectively excluding the region of lowest signal to background ratio containing the bulk of the DY background. The E_T^{miss} distribution after all cuts except the one on the MET is shown in fig. 5.5. No significant excess in data hinting at new physics can be observed. After an exemplary MET cut at 150 GeV is applied, 83 events are observed in data and 94.2 ± 2.6(stat.) MC events are predicted.

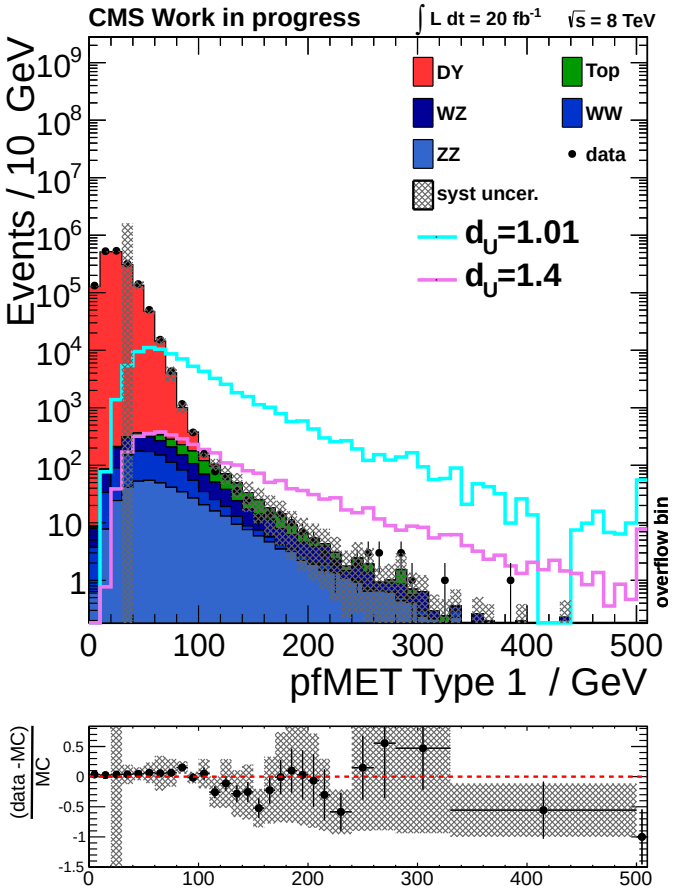

Figure 5.5.: The final distribution of the missing transverse energy with all cuts except MET cut applied. The huge systematic uncertainty at about 30 GeV (outside of the signal region) is due to some error in the plotting method.

5.7. Corrections & Systematic Uncertainties

In complex experiments that are exploring new physics, it is difficult to predict every detail to a high precision in advance. So it comes as no surprise that MC samples and real data slightly differ on some points. Most notably on the number of expected pile-up events, the jet resolution and the ϕ distribution of the missing transverse energy. All of these issues are corrected as described below.

Another important element in the comparison of MC prediction and data are the systematic uncertainties. There are two categories: global uncertainties, that affect an event as a whole (cross sections, PDFs, luminosity), and object related uncertainties (resolution, scale) relevant to the objects in the event individually. As the missing transverse energy is calculated using all the other objects in the event, their uncertainties have to be propagated into the MET uncertainty accordingly.

5.7.1. Pile-up Reweighting

As the protons circulate in bunches, there is almost always more than just one collision of two protons at the interaction point. Those extra pile-up collisions add objects to the event that have to be considered. Even slow decays from a previous bunch crossing can sometimes be detected - called out-of-time pile-up.

In the production of the MC samples, a minimum bias sample is used to simulate the expected underlying pile-up events. However, the assumed distribution of the number of those events does not completely match that of the measured data. The ratio of the normalized real distribution and the normalized production distribution provides values that are used to reweight every MC event according to its true number of interactions. In the process of calculating the distribution for the real data used in the analysis, the total inelastic cross section can be varied for fine tuning. As suggested in [50] a value of $\sigma = 73.5\,\text{mb}$ for processes with $Z \to \mu\mu$ is used instead of the default 69.4 mb.

For the uncertainty, the true number of interactions is shifted up and down by a recommended value [51] of 5 % before the weight is calculated. To account for the deviation in the cross section, the weight is also evaluated for $\sigma = 69.4\,\text{mb}$. The difference between these three and the initial weight is determined and the maximum taken as the uncertainty.

5.7.2. Jet Smearing

Another known issue is the resolution of the jet p_T. In MC, it is better than in the experiment. To balance the difference, the MC jets are smeared. If the reconstructed jet can be matched to a jet on generator level, the formula [52] for the calculation of the scaled $\tilde{p}_T$ is:

$$\tilde{p}_T = \max(0, p_T^{gen} + c \cdot (p_T - p_T^{gen})), \tag{5.5}$$

where p_T^{gen} is the transverse momentum of the matched generated jet and c is an η dependent scaling factor. With $1.052 \leq c \leq 1.288$ the new difference between reconstructed and generated p_T is always greater than before thus decreasing the resolution.

Jets, which can not be matched to a generator level jet, are randomly smeared using a Gaussian with a standard deviation of

$$\sigma = \sqrt{c^2 - 1} \cdot \sigma_{MC}, \tag{5.6}$$

where c is the same scaling factor as before and σ_{MC} is the jet resolution in simulation. It is derived from the resolution of matched jets with equivalent transverse momentum.

5.7.3. MET x/y shift correction

Both real and simulated data show a modulation in the ϕ distribution of the missing transverse energy (see fig. B.1). This is caused by a systematic shift of the x and y components of the MET. The shift is proportional to the number of reconstructed vertices N_{vtx}, but it is not the same for data and MC. Because of that the following correction [53] is applied to CMS data with different factors c_0 and c_1 for both cases:

$$\begin{aligned} \tilde{E}_x^{miss} &= E_x^{miss} + c_{0,x} + c_{1,x} \cdot N_{vtx} \\ \tilde{E}_y^{miss} &= E_y^{miss} + c_{0,y} + c_{1,y} \cdot N_{vtx} \end{aligned}$$

to reach a better agreement of the corrected ϕ distributions.

5.7.4. Lepton Resolution & Scale

To account for the influence of the lepton measurement on the missing transverse energy, the muon and electron momenta are shifted and smeared before they are

propagated into the MET. The resolution uncertainty is applied by smearing the components of the lepton $\vec{p}$ using a Gaussian with the value of the uncertainty σ_{res} as the standard deviation. By shifting the components of the momentum up and down with

$$\tilde{p}_\alpha = (1 \pm \sigma_{scale}) \cdot p_\alpha, \tag{5.7}$$

the scale uncertainty is taken into account. In each case the differences between the old and new p components are used to correct the E_T^{miss}.

The uncertainties on the momentum resolution and scale of muons were estimated for $\sqrt{s} = 7\,\text{TeV}$ [54]. In data from the decay $Z \to \mu\mu$, the invariant mass of the two muons was used to reconstruct the Z mass peak. By comparing different fits to the peak, values for the uncertainties were derived. The recommended [55] values for the uncertainty on the resolution $\sigma_{res} = 0.6\,\%$ and the scale $\sigma_{scale} = 0.2\,\%$ are based on this study.

For the electron scale, different values for barrel (1.3 %) and endcap (4.1 %) [56] are used. The electron momentum resolution uncertainty is estimated to be 0.6 %.

5.7.5. Jet Resolution

As described in sec. 5.7.2, the jet resolution is already smeared to correct for the difference in resolution between MC and data. The same method is applied to calculate the corresponding uncertainties. The formulas 5.5 and 5.6 are used for matched and unmatched jets respectively, but this time the scaling factor c is shifted up and down by its error σ_c found in [52].

5.7.6. Jet Energy Scale

The Type-I correction of the missing transverse energy already propagates the influence of the jet energy scale as part of the MET reconstruction (see sec. 4.5). Just like with the jet resolution the uncertainty on the jet energy scale depends on the pseudorapidity and momentum of the jet. The implementation is the same as for the lepton scale using formula 5.7, but instead of a constant σ_{scale} values from tables [57] are used according to η and p_T.

5.7.7. Luminosity

There are different ways to determine the luminosity from measurements (see sec. 3.3.7) with the CMS detector. The pixel cluster counting method results in an integrated luminosity of $L = 19.7 \pm 0.5\,\mathrm{fb}^{-1}$ for the full 2012 pp dataset [25]. This gives an uncertainty of 2.6 %. As the MC samples are all scaled to the data luminosity, the uncertainty has to be taken into account for every single one.

5.7.8. MC Cross Sections

As equation 3.4 states, the number of expected events solely depends on the integrated luminosity and the process cross section. Since cross sections are only known within uncertainties, their influence on the event numbers has to be considered. In tab. 5.1 the cross sections are listed. The uncertainties are taken from [41] as far as they are available. They consist of scale uncertainties and PDF uncertainties. The former are determined by varying the factorisation and renormalisation scale, which are assumed to be fully correlated, by a factor 2 up and down.

Since the $t\bar{t}$ background is the dominant one in the signal region of the MET distribution, its cross section uncertainty has the biggest influence on the overall uncertainty.

5.7.9. PDF Uncertainties

Parton distribution functions give the probability for a parton of a certain energy fraction x and momentum transfer Q of the proton energy. Several groups produce PDF sets obtained from experimental data while assumptions on the theory are taken into account. In a set, the best fit to the PDF is provided along with parameter variations that can be used to calculate uncertainties. Since there is no theoretical prediction for a correct PDF set, it is recommended [58] to evaluate different PDF sets and derive appropriate uncertainties. The most accurate way for comparison would be to produce every MC sample multiple times with different PDFs. A faster and less computing intensive approach is to perform a reweighting of the events. The corresponding weights are calculated comparing the original production PDF set CTEQ6L (CT10 for the $t\bar{t}$ samples) to the PDF sets NNPDF2.2 and MSTW2008. Following the recipe in [59], the PDF uncertainties can be calculated with:

$$\sigma(PDF,+) = \frac{1}{C_{90}}\sqrt{\sum_{i=1}^{N/2}(\max \mathcal{O}[q^{(2i-1)}] - \mathcal{O}[q^{(0)}], \mathcal{O}[q^{(2i)}] - \mathcal{O}[q^{(0)}], 0)^2} \tag{5.8}$$

$$\sigma(PDF,-) = \frac{1}{C_{90}}\sqrt{\sum_{i=1}^{N/2}(\max \mathcal{O}[q^{(0)}] - \mathcal{O}[q^{(2i-1)}], \mathcal{O}[q^{(0)}] - \mathcal{O}[q^{(2i)}], 0)^2}, \tag{5.9}$$

where N is the number of members in a PDF set ($i = 0$ representing the best fit) and C_{90} a factor used to rescale CTEQ to an 68 % confidence level.

An uncertainty on the strong coupling constant α_s is also provided in a PDF set as it influences the global fit to the PDF. Both uncertainties can be combined by summing them in quadrature.

The NNPDF2.2 set uses a different approach. More details and the formulas can also be found in [59].

5.7.10. Summary of the Uncertainties

The influence of the different uncertainties on the number of events in the E_T^{miss} distribution is shown in table 5.5. For the signal samples, only the muon resolution has a noticeable impact.

	background	signal
pile-up	3 %	1 %
jet resolution	4 %	1 %
jet scale	4 %	1 %
μ resolution	4 %	4 %
μ scale	4 %	1 %
e resolution	3 %	1 %
e scale	4 %	1 %
PDF	3 %	1 %
cross section	4 %	-
luminosity	2.6 %	

Table 5.5.: Summary of all systematic uncertainties on the number of events after the cuts are applied. The MET cut is here set to 100 GeV.

5.8. Cut Optimisation

While cuts on discrete values such as the number of jets are easily motivated, there often is no obvious choice for the cut value on a continuous distribution. To decide on a suitable cut a method for optimisation is applied. In the process, expected limits for a single bin counting experiment are calculated over a whole range of possible cut values to find the best one. For more details, see sec. 6 explaining the final limit calculation.

In case of the response cut, which uses missing transverse energy in its definition, an estimated cut of $E_T^{miss} > 100\,\text{GeV}$ is applied before the optimisation. This is done to study the influence of a change in MET on the optimal cut for the response independent from other cuts. The corresponding distribution of the response after the MET cut is shown in fig. 5.6. A region of $-2.0 < u_{||}/p_T^Z < 0.75$ is tested (see fig. 5.7(a)). The optimal cut is at $u_{||}/p_T^Z = -0.3$. Varying the MET cut does not significantly change it.

This optimisation is also used for the final distribution of the missing transverse energy after all other cuts described in sec. 5.6 are applied. Limits are calculated for $70\,\text{GeV} < E_T^{miss} < 390\,\text{GeV}$. As shown in fig. 5.7(b), the optimal cut values are not close enough together for the different signal samples. So, instead of one universal cut the individual values listed in tab. 6.1 are used in the limit calculation.

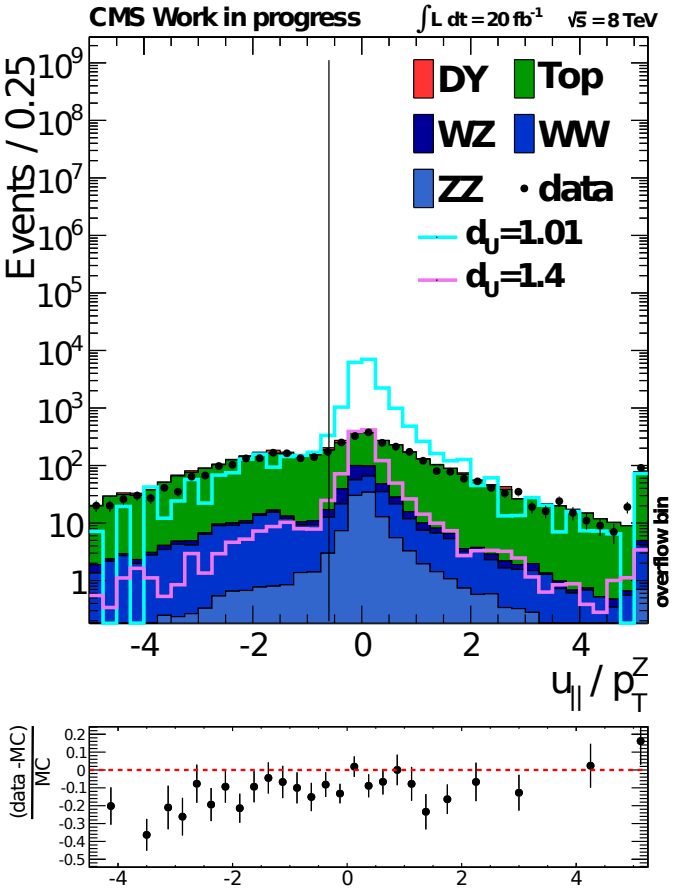

Figure 5.6.: Response with only the MET cut applied, testing the influence of MET on the response. The cut is only optimised on one side (left).

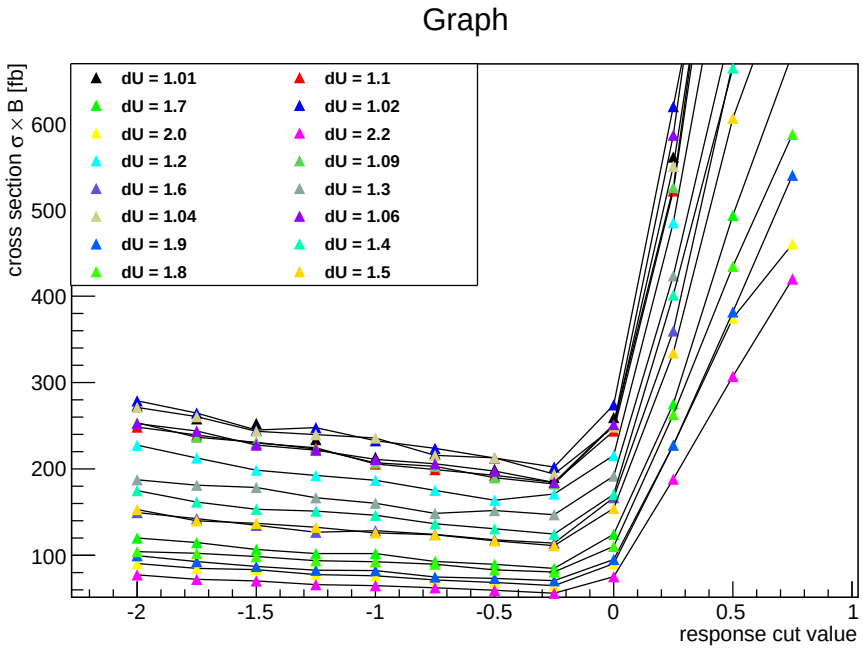

(a) Expected limits as function of the applied cut on the response for the different $d_{\mathcal{U}}$. A minimum close to -0.3 can be seen for all curves.

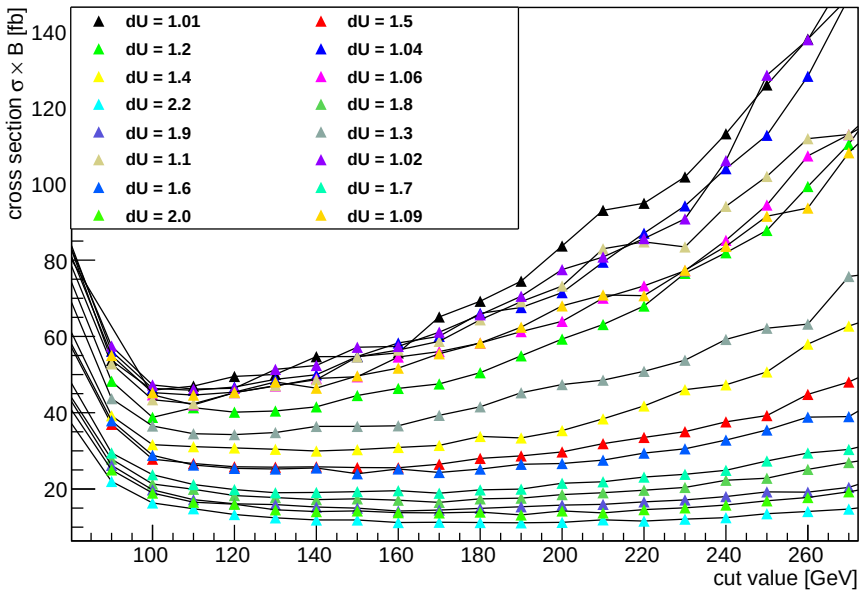

(b) Expected limits as function of the applied cut on E_T^{miss} for the different $d_{\mathcal{U}}$. For higher $d_{\mathcal{U}}$, the curves tend to have a broader minimum at higher MET.

Figure 5.7.: Plots of the optimisation for: (a) response cut, (b) MET cut.

6. Results

The search for new physics can either result in a discovery (e.g. with significant excess in data) or the Standard Model prediction and the data are in good agreement. In case of the latter, exclusion limits can be calculated. In this analysis, upper limit are set on the cross section for the signal production depending on the unparticle dimension $d_{\mathcal{U}}$.

6.1. Statistics

In statistics, there are two main approaches to the concept of probability [4]. In frequentist statistics, probability is interpreted as the frequency of the outcome of a repeatable experiment. The framework provides tools for parameter estimation and construction of confidence intervals, which contain the true parameter value within a given probability. This approach is widely used to objectively report measurements and the corresponding statistical uncertainties.

In the Bayesian approach, the degree of belief plays an important role and leads to a more subjective probability. The probability density function (p.d.f.) of a parameter contains prior assumptions about its true value. Bayesian methods always require the prior p.d.f. as input for the parameters, but additional information can easily be added. Also systematic uncertainties are well handled with Bayesian statistics.

Here, a combination of both is used, Bayesian limit calculation and a frequentist confidence level method.

6.2. The CL_s Method

In order to quantify the signal exclusion limits, confidence levels are calculated. In the CL_s method two hypotheses are considered: it is common to choose the Standard Model background as the prediction of a null-hypothesis H_0 which is supposed to be refuted in favour of another hypothesis H_1 predicting a combination of signal and background. In order to calculate the corresponding confidences CL_b and CL_{s+b}, the

following formulas [60] with test-statistic Q and the experimentally observed value Q_{obs} are used:

$$CL_i = P_i(Q \leq Q_{obs}) = \int_{-\infty}^{Q_{obs}} \frac{dP_i}{dQ} dQ, \quad i = \{b, s+b\}, \tag{6.1}$$

where $\frac{dP_i}{dQ}$ is the probability distribution function (p.d.f.) of the test-statistic.
Finally, the modified frequentist re-normalisation:

$$CL_s = \frac{CL_{s+b}}{CL_b}, \tag{6.2}$$

gives the confidence of the signal and is used to exclude the signal hypothesis at the confidence level (CL):

$$1 - CL_s \leq CL. \tag{6.3}$$

In this analysis, a CL of 95 % is used. For the upper limit on the signal cross section, only 5 % of the pseudo-experiments result in values above the given exclusion limit.

6.3. Profile Likelihood

In the single bin counting experiment, only the total number of events above the cut on E_T^{miss} is considered. The likelihood ratio is [4]:

$$Q = \frac{\mathcal{L}(s+b, n)}{\mathcal{L}(b, n)}, \tag{6.4}$$

with a Poisson distributed likelihood $\mathcal{L}(\mu, n) = \frac{\mu^n}{n!} e^{-\mu}$ to find n events where μ are expected. This frequentist definition only considers statistical uncertainties. To also include systematic uncertainties, the likelihood is multiplied with a Bayesian prior function for every parameter uncertainty leading to the profile likelihood:

$$\mathcal{L}(\mu, n, \theta) = \mathcal{L}(\mu, n) \prod_i \pi_i(\theta_i). \tag{6.5}$$

The priors are modelled with log-normal functions. In pseudo-experiments the number of events n (Poisson) and the nuisance parameter θ (based on p.d.f.) are randomly generated and Q is evaluated for the limit calculation.

6.4. Limit Calculation Results

The RooStats [61] based statistics tool Higgs-Combine [62] is used to calculate the exclusion limits that are shown in fig. 6.1(a). The expected and observed limits are listed in tab. 6.1.

The free parameters in the unparticle theory are $d_{\mathcal{U}}$, $\Lambda_{\mathcal{U}}$ and λ. With the coupling constant set to $\lambda = 1$, the calculated cross section limits can be translated into a $\Lambda_{\mathcal{U}}$-$d_{\mathcal{U}}$ plane shown in fig. 6.1(b). The parameter space below a curve is excluded for that particular channel. As $d_{\mathcal{U}}$ approaches 1, the cross section becomes independent of $\Lambda_{\mathcal{U}}$ (see equation 5.2) and very high values of $\Lambda_{\mathcal{U}}$ can therefore be excluded. Tab. 6.2 shows the limits on the unparticle dimension $d_{\mathcal{U}}$ depending on the cut off parameter $\Lambda_{\mathcal{U}}$. They substantially improve both the 2011 analysis in the same channel [63] as well as complementary monojet results using the 2012 data [64].

$d_{\mathcal{U}}$	MET cut / GeV	Obs. limit / fb	Exp. limit / fb
1.01	100	31	44
1.02	110	25	48
1.04	110	25	48
1.06	110	23	45
1.09	110	23	45
1.10	110	23	43
1.20	100	27	41
1.30	120	23	35
1.40	140	20	30
1.50	160	28	26
1.60	150	17	26
1.70	170	21	19
1.80	170	19	18
1.90	160	16	15
2.00	190	13	14
2.20	190	10	11

Table 6.1.: Expected and observed 95 % CL upper limits on the cross section σ for scalar unparticles at a fixed coupling constant $\lambda = 1$. The lower MET cuts are optimised for the best expected limit.

$\Lambda_{\mathcal{U}}$ / TeV	obs. $d_{\mathcal{U}}$	exp. $d_{\mathcal{U}}$
1	2.17	2.16
2	1.94	1.94
3	1.86	1.87
5	1.78	1.79
10	1.69	1.7
15	1.67	1.66
20	1.65	1.62
50	1.57	1.55
80	1.5	1.51
100	1.5	1.5
1000	1.41	1.4

Table 6.2.: Expected and observed limits on the unparticle dimension for scalar unparticles at a fixed coupling constant $\lambda = 1$.

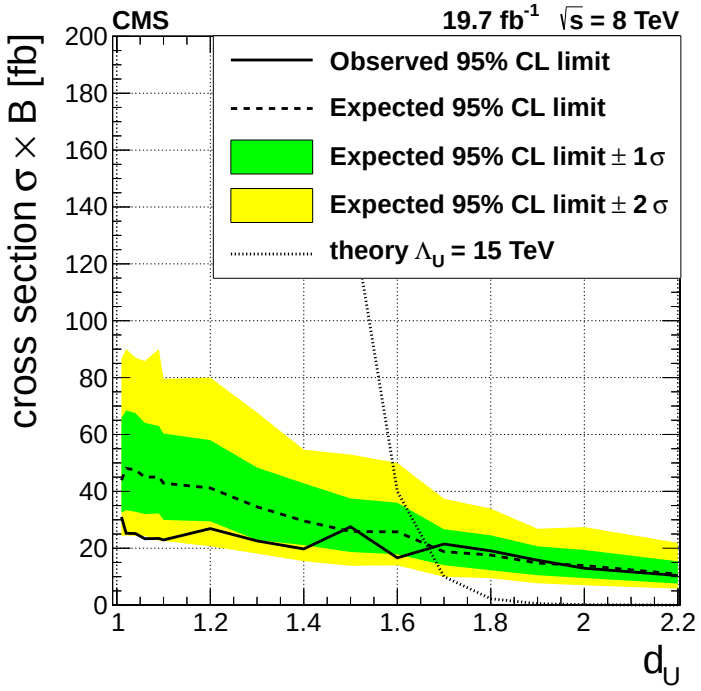

(a) Expected and observed 95 % CL upper limits on cross section σ for scalar unparticles at a fixed coupling constant $\lambda = 1$ as function of $d_{\mathcal{U}}$.

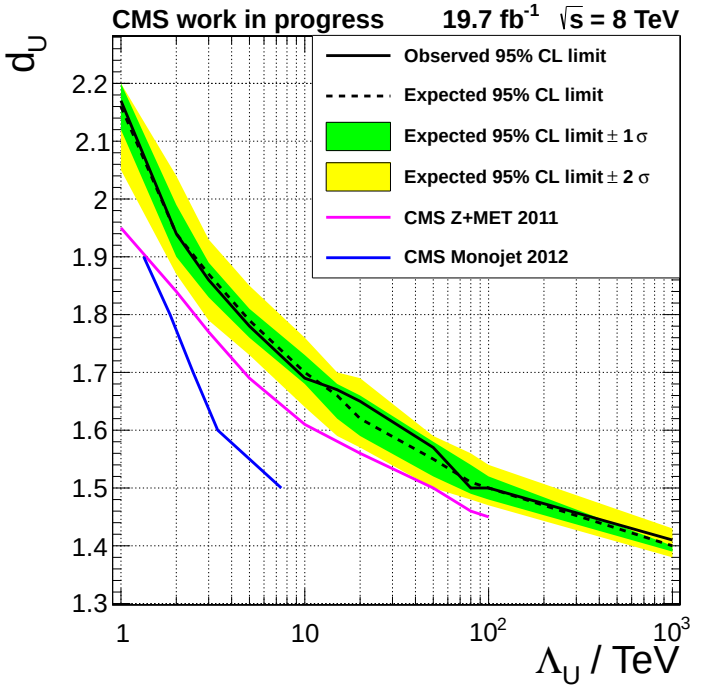

(b) Limits translated into the $\Lambda_{\mathcal{U}}$-$d_{\mathcal{U}}$ plane for a fixed coupling constant $\lambda = 1$ in comparison to CMS Monojet limits using the 2012 data [64] and previous Z+MET limits ($\sqrt{s} = 7$ TeV) [63].

Figure 6.1.: (a) Exclusion limits on the cross section, (b) limits translated into the $\Lambda_{\mathcal{U}}$-$d_{\mathcal{U}}$ plane.

7. Conclusion

This thesis presents a search for unparticles in the channel Z + MET in data taken at the CMS experiment. The full 2012 dataset of proton proton collisions at a center of mass energy of $\sqrt{s} = 8\,\text{TeV}$ was analysed, corresponding to an integrated luminosity of $L = 19.7\,\text{fb}^{-1}$. MC signal samples have been produced for different parameter points and background processes with a similar signature were chosen for further analysis.

As unparticles themselves are not directly detectable, the missing transverse energy was chosen as the main distribution for comparing signal and background to data. Cuts on prominent signal properties were introduced to reduce the background contribution.

Because no significant excess in data could be observed in the signal region of high missing transverse energy, exclusion limits were calculated taking systematic uncertainties on the objects into account.

The exclusion area for $d_{\mathcal{U}}$ has been expanded from $d_{\mathcal{U}} = 1.41$ at $\Lambda_{\mathcal{U}} = 1000\,\text{TeV}$ to $d_{\mathcal{U}} = 2.17$ at $\Lambda_{\mathcal{U}} = 1\,\text{TeV}$. The limits were improved compared to a previous search in the same channel at $\sqrt{s} = 7\,\text{TeV}$ by a factor of about 2, as well as compared to the monojet search at CMS by factor of 2 to 3.

A. Conventions

- In an effort to simplify calculations in particle physics, it is common to use natural units, where the natural constants

$$c = \hbar = 1. \tag{A.1}$$

  That way quantities of mass, momentum and energy can all be given in units of electron Volt (eV).
- Cross sections are given in barn: $1\,\mathrm{b} = 10^{-28}\,\mathrm{m}^2$
- Z and W denote the gauge bosons Z^0 and $\mathrm{W}^{\pm}$.
- Antimuon and muon both are synonymously named muon, just like electrons and positrons are simply referred to as electrons.

B. Supporting plot for MET ϕ correction

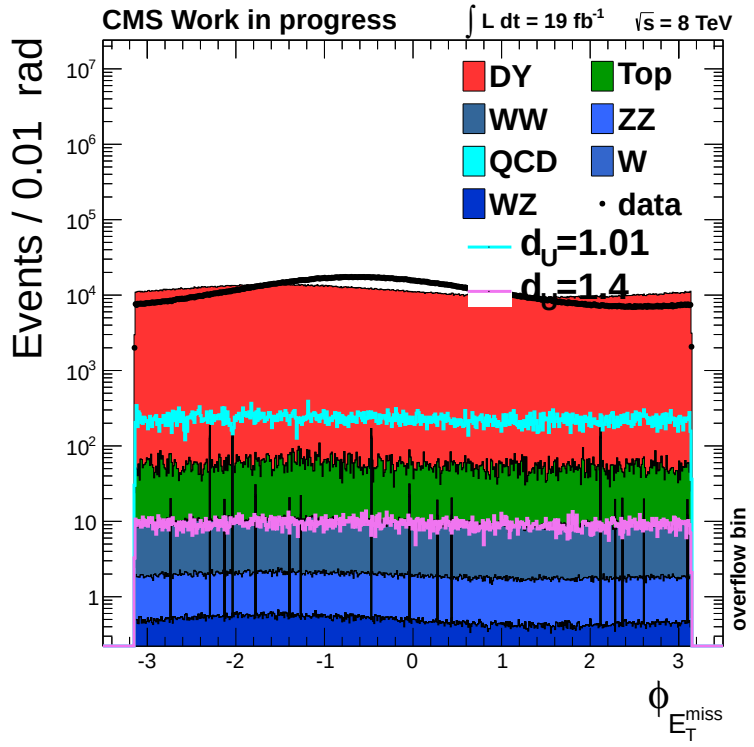

Figure B.1.: Early plot of the MET ϕ distribution without MET x/y shift correction. Different modulations in data and MC are clearly visible.

C. Plots of the cut flow

Shown in fig. C.1 is the E_T^{miss} distribution at the different steps of the cut based analysis.

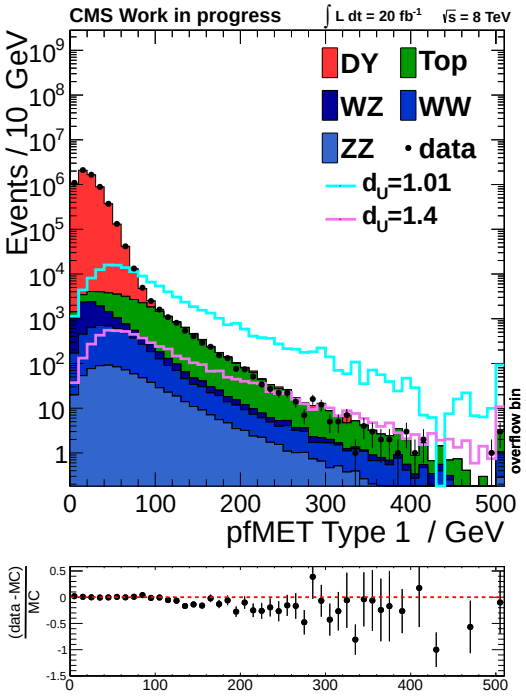

(a) MET after event selection

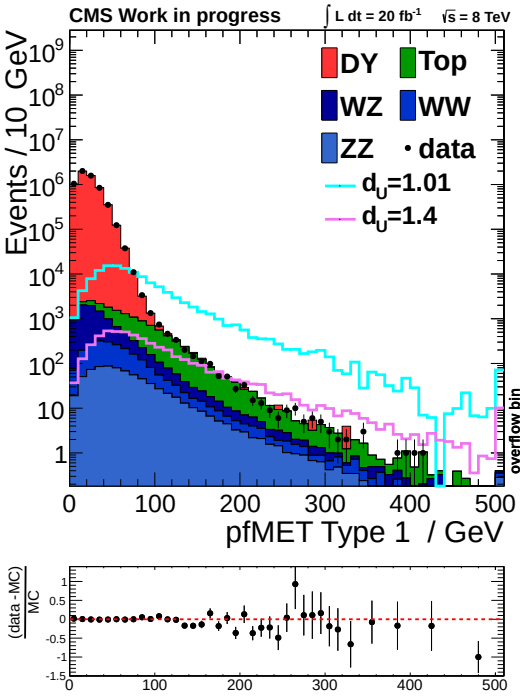

(b) MET after Z mass cut

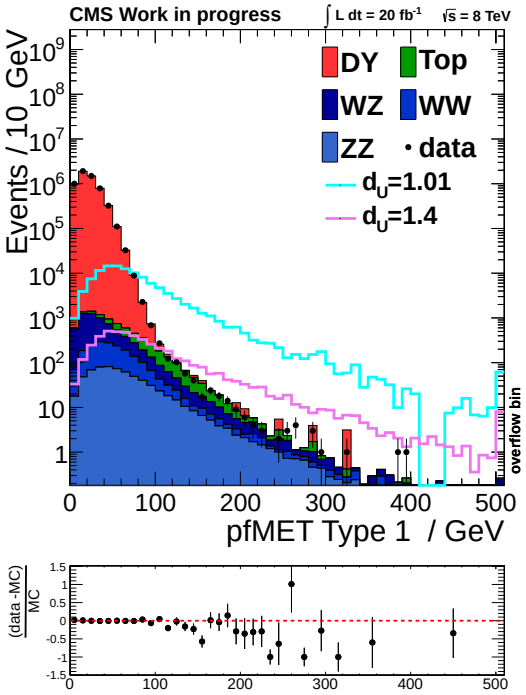

(c) MET after jet multiplicity cut

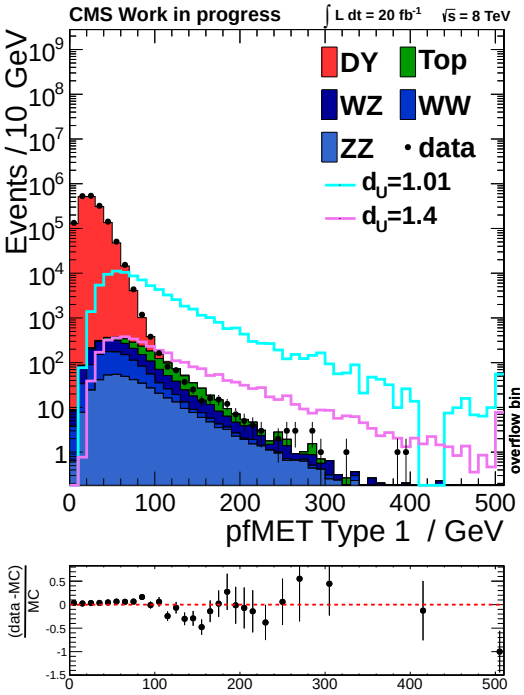

(d) MET after response cut

Figure C.1.: Display of the different cut stages of the MET distribution

D. Event Display

A possible candidate for an unparticle in CMS data is displayed in figure D.1. The event (run number:207269, luminosity section:181, event number:219613713) matches the requirements of the associated production of Z and $\mathcal{U}$. Two muons and high missing transverse energy ($E_T^{miss} = 392\,\text{GeV}$) are detected almost back to back.

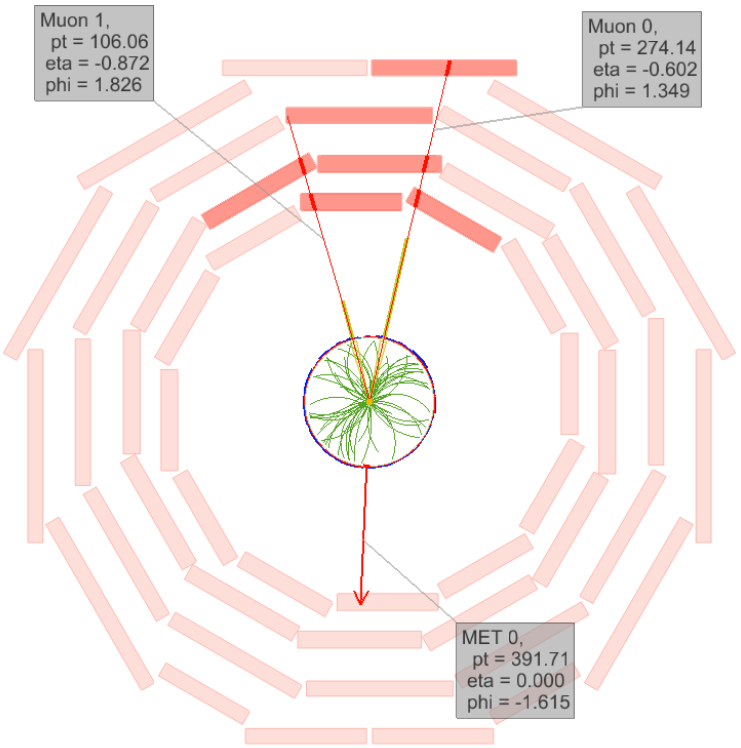

Figure D.1.: The CMS event display shows a data event that passed all selection cuts. Two muons are seen in the r-ϕ plane opposite of very high MET of 392 GeV.

List of Figures

List of Tables

Bibliography

[1] H. Georgi, "Unparticle physics", *Physical review letters* (March, 2007) 9, arXiv:0703260. doi:10.1103/PhysRevLett.98.221601.

[2] D. Griffith, "Introduction to Elementary Particles". WILEY-VCH Verlag GmbH & Co. KGaA, Weinheim, 2008.

[3] Wikipedia Collaboration, "Standard Model of Elementary Particles". http://en.wikipedia.org/wiki/File:Standard_Model_of_Elementary_Particles.svg accessed on 09/22/2013.

[4] Particle Data Group Collaboration, "The Review of Particle Physics", *Phys. Rev. D86* (2012).

[5] J.-F. Fortin, B. Grinstein, and A. Stergiou, "Cyclic unparticle physics", *Physics Letters B* **709** (March, 2012) 408–412, arXiv:arXiv:1110.1634v1. doi:10.1016/j.physletb.2012.02.046.

[6] H. Georgi, "Another odd thing about unparticle physics", *Physics Letters B* **650** (July, 2007) 275–278, arXiv:0704.2457v2. doi:10.1016/j.physletb.2007.05.037.

[7] H. Georgi and Y. Kats, "Unparticle Example in 2D", *Physical Review Letters* **101** (September, 2008) 131603, arXiv:arXiv:0805.3953v1. doi:10.1103/PhysRevLett.101.131603.

[8] K. Cheung, W.-y. Keung, and T.-c. Yuan, "Collider phenomenology of unparticle physics", *Physical Review D* **76** (September, 2007) 055003, arXiv:arXiv:0706.3155v2. doi:10.1103/PhysRevD.76.055003.

[9] S. Ask, I. Akin, L. Benucci et al., "Real emission and virtual exchange of gravitons and unparticles in Pythia8", *Computer Physics Communications* **181** (September, 2010) 1593–1604, arXiv:0912.4233v2. doi:10.1016/j.cpc.2010.05.013.

[10] B. Grinstein, K. Intriligator, and I. Z. Rothstein, "Comments on unparticles", *Physics Letters B* **662** (May, 2008) 367–374, arXiv:arXiv:0801.1140v2. doi:10.1016/j.physletb.2008.03.020.

[11] A. Delgado, J. R. Espinosa, and M. Quirós, "Unparticles-Higgs interplay", *Journal of High Energy Physics* **2007** (October, 2007) 094–094, arXiv:arXiv:0707.4309v2. doi:10.1088/1126-6708/2007/10/094.

[12] D. Stancato and J. Terning, "The Unhiggs", *Journal of High Energy Physics* **2009** (November, 2009) 101–101, arXiv:arXiv:0807.3961v2. doi:10.1088/1126-6708/2009/11/101.

[13] T. Kikuchi and N. Okada, "Unparticle dark matter", *Physics Letters B* **665** (July, 2008) 186–189, arXiv:arXiv:0711.1506v3. doi:10.1016/j.physletb.2008.06.021.

[14] J. Bergström and T. Ohlsson, "Unparticle self-interactions at the Large Hadron Collider", *Physical Review D* **80** (December, 2009) 115014, arXiv:arXiv:0909.2213v2. doi:10.1103/PhysRevD.80.115014.

[15] A. Delgado, J. Espinosa, J. No et al., "Note on unparticle decays", *Physical Review D* **79** (March, 2009) 055011, arXiv:arXiv:0812.1170v1. doi:10.1103/PhysRevD.79.055011.

[16] J. Feng, A. Rajaraman, and H. Tu, "Unparticle self-interactions and their collider implications", *Physical Review D* **77** (April, 2008) 075007, arXiv:arXiv:0801.1534v2. doi:10.1103/PhysRevD.77.075007.

[17] A. Delgado and M. J. Strassler, "Simple-minded unitarity constraint and an application to unparticles", *Physical Review D* **81** (March, 2010) 056003, arXiv:arXiv:0912.2348v1. doi:10.1103/PhysRevD.81.056003.

[18] L. Evans and P. Bryant, "LHC machine", *Journal of Instrumentation* **3** (August, 2008) S08001–S08001. doi:10.1088/1748-0221/3/08/S08001.

[19] ATLAS Collaboration, "The ATLAS Experiment at the CERN Large Hadron Collider", *Journal of Instrumentation* **3** (August, 2008) S08003–S08003. doi:10.1088/1748-0221/3/08/S08003.

[20] LHCb Collaboration, "The LHCb Detector at the LHC", *Journal of Instrumentation* **3** (August, 2008) S08005–S08005. doi:10.1088/1748-0221/3/08/S08005.

[21] ALICE Collaboration, "The ALICE experiment at the CERN LHC", *Journal of Instrumentation* **3** (August, 2008) S08002–S08002. doi:10.1088/1748-0221/3/08/S08002.

[22] CMS Collaboration, "The CMS experiment at the CERN LHC", *Journal of Instrumentation* **3** (August, 2008) S08004–S08004. doi:10.1088/1748-0221/3/08/S08004.

[23] CMS Collaboration, "The CMS Tracker System Project", *CMS Technical Design Report* **CMS-TDR-005** (1997).

[24] CMS Collaboration, "CMS Physics: Technical Design Report Volume 1: Detector Performance and Software", *CMS Technical Design Report* **CMS TDR-8-1** (2006).

[25] CMS Collaboration, "CMS Luminosity Based on Pixel Cluster Counting - Summer 2013 Update", *CMS Physics Analysis Summary* **CMS PAS LUM-13-001** (2013).

[26] WLCG Collaboration, "Worldwide LHC Computing Grid". http://wlcg.web.cern.ch accessed on 08/15/2013.

[27] CMS Collaboration, "CMS Twiki: CMSSW Application Framework". https://twiki.cern.ch/twiki/bin/view/CMSPublic/WorkBookCMSSWFramework accessed on 08/15/2013.

[28] "ROOT - An Object Oriented Data Analysis Framework". http://root.cern.ch/ accessed on 08/15/2013.

[29] C. Magass et al., "ACSusyAnalysis Software Package". https://twiki.cern.ch/twiki/bin/view/ACSusyAnalysis/ accessed on 08/19/2013.

[30] CMS Collaboration, "Particle-Flow Event Reconstruction in CMS and Performance for Jets, Taus, and MET", *CMS Physics Analysis Summary* **CMS PAS PFT-09-001** (2009).

[31] S. Cucciarelli, M. Konecki, D. Kotlinski et al., "Track reconstruction, primary vertex finding and seed generation with the Pixel Detector", *CMS Note* **CMS Note 2006_026** (2006).

[32] R. Frühwirth, "Application of Kalman filtering to track and vertex fitting", *Nuclear Instruments and Methods in Physics Research Section A: Accelerators,*

Spectrometers, Detectors and Associated Equipment **262** (December, 1987) 444–450. doi:10.1016/0168-9002(87)90887-4.

[33] S. Baffioni, C. Charlot, F. Ferri et al., "Electron reconstruction in CMS", *CMS Note* **CMS Note 2006_040** (2006).

[34] W. Adam, R. Frühwirth, A. Strandlie et al., "Reconstruction of Electrons with the Gaussian-Sum Filter in the CMS Tracker at the LHC", *CMS Note* **CMS Note 2005_001** (2005).

[35] M. Cacciari, G. P. Salam, and G. Soyez, "The anti-k_t jet clustering algorithm", *Journal of High Energy Physics* **2008** (April, 2008) 063–063, arXiv:arXiv:0802.1189v2. doi:10.1088/1126-6708/2008/04/063.

[36] CMS Collaboration, "Missing E_T performance", *CMS Physics Analysis Summary* **CMS PAS JME-07-001** (2007).

[37] T. Sjöstrand, S. Mrenna, and P. Skands, "PYTHIA 6.4 physics and manual", *Journal of High Energy Physics* **2006** (May, 2006) 026–026, arXiv:0603175. doi:10.1088/1126-6708/2006/05/026.

[38] S. Frixione, P. Nason, and C. Oleari, "Matching NLO QCD computations with parton shower simulations: the POWHEG method", *Journal of High Energy Physics* **2007** (November, 2007) 070–070, arXiv:arXiv:0709.2092v1. doi:10.1088/1126-6708/2007/11/070.

[39] J. Alwall, M. Herquet, F. Maltoni et al., "MadGraph 5: going beyond", *Journal of High Energy Physics* **2011** (June, 2011) 128, arXiv:1106.0522. doi:10.1007/JHEP06(2011)128.

[40] S. Agostinelli, J. Allison, K. Amako et al., "Geant4—a simulation toolkit", *Nuclear Instruments and Methods in Physics Research Section A: Accelerators, Spectrometers, Detectors and Associated Equipment* **506** (July, 2003) 250–303. doi:10.1016/S0168-9002(03)01368-8.

[41] CMS Collaboration, "CMS Twiki: Standard Model Cross Sections for CMS at 8 TeV". https://twiki.cern.ch/twiki/bin/view/CMS/StandardModelCrossSectionsat8TeV accessed on 09/18/2013.

[42] CMS Collaboration, "CMS Twiki: Standard Model Cross Sections for CMS at 7 TeV". https://twiki.cern.ch/twiki/bin/view/CMS/StandardModelCrossSections accessed on 09/20/2013.

[43] T. Sjöstrand, S. Mrenna, and P. Skands, "A brief introduction to PYTHIA 8.1", *Computer Physics Communications* **178** (June, 2008) 852–867, arXiv:arXiv:0710.3820v1. doi:10.1016/j.cpc.2008.01.036.

[44] S. Ask, "Simulation of Z plus graviton/unparticle production at the LHC", *The European Physical Journal C* **60** (February, 2009) 509–516, arXiv:0809.4750. doi:10.1140/epjc/s10052-009-0949-7.

[45] CMS Collaboration, "CMS Twiki: SWGuide Muon ID". https://twiki.cern.ch/twiki/bin/view/CMSPublic/SWGuideMuonId accessed on 08/22/2013.

[46] CMS Collaboration, "CMS Twiki: Cut Based Electron ID". https://twiki.cern.ch/twiki/bin/view/CMS/EgammaCutBasedIdentification accessed on 08/24/2013.

[47] CMS Collaboration, "CMS Twiki: Jet Identification". https://twiki.cern.ch/twiki/bin/view/CMS/JetID accessed on 08/26/2013.

[48] CMS Collaboration, "CMS Twiki: MET Optional Filters". https://twiki.cern.ch/twiki/bin/view/CMS/MissingETOptionalFilters accessed on 08/26/2013.

[49] CMS Collaboration, "Performance of b tagging at sqrt(s)=8 TeV in multijet, ttbar and boosted topology events", *CMS Physics Analysis Summary* **CMS PAS BTV-13-001** (2013).

[50] CMS Collaboration, "CMS Twiki: Utilities for Accessing Pileup Information for Data". https://twiki.cern.ch/twiki/bin/view/CMS/PileupJSONFileforData accessed on 09/12/2013.

[51] CMS Collaboration, "CMS Twiki: Estimating Systematic Errors Due to Pileup Modeling". https://twiki.cern.ch/twiki/bin/view/CMS/PileupSystematicErrors accessed on 09/18/2013.

[52] CMS Collaboration, "CMS Twiki: Jet Energy Resolution Measurement". https://twiki.cern.ch/twiki/bin/view/CMS/JetResolution accessed on 09/12/2013.

[53] CMS Collaboration, "CMS Twiki: MET Analysis - MET x/y Shift Correction (for ϕ modulation)". `https://twiki.cern.ch/twiki/bin/view/CMSPublic/WorkBookMetAnalysis#MET_x_y_Shift_Correction_for_mod` accessed on 09/14/2013.

[54] CMS Collaboration, "Performance of muon reconstruction and identification in pp collisions at $\sqrt{s}$=7 TeV", *CMS Physics Analysis Summary* **CMS PAS MUO-10-004** (2011).

[55] CMS Collaboration, "CMS Twiki: Reference muon momentum scale and resolution". `https://twiki.cern.ch/twiki/bin/view/CMS/MuonReferenceResolution` accessed on 09/20/2013.

[56] CMS Collaboration, "Search for excited leptons in pp Collisions at $\sqrt{s}$=7 TeV", *CMS Physics Analysis Summary* **CMS PAS EXO-10-016** (2010).

[57] CMS Collaboration, "CMS Twiki: Jet energy scale uncertainty sources". `https://twiki.cern.ch/twiki/bin/view/CMS/JECUncertaintySources` accessed on 09/21/2013.

[58] M. Botje, J. Butterworth, A. Cooper-Sarkar et al., "The PDF4LHC Working Group Interim Recommendations", `arXiv:1101.0538`.

[59] PDF4LHC Collaboration, "Practical implementation of the PDF4LHC recipe". `http://www.hep.ucl.ac.uk/pdf4lhc/PDF4LHC_practical_guide.pdf/` accessed on 09/24/2013.

[60] A. L. Read, "Modified frequentist analysis of search results (the CL_s method)", *1st Workshop on Confidence Limits* (January, 2000) 81–101.

[61] CMS Collaboration, "CMS Twiki: RooStats page in CMS Twiki". `https://twiki.cern.ch/twiki/bin/view/CMS/RooStats` accessed on 09/21/2013.

[62] CMS Collaboration, "CMS Twiki: Documentation of the RooStats-based statistics tools for Higgs PAG". `https://twiki.cern.ch/twiki/bin/view/CMS/SWGuideHiggsAnalysisCombinedLimit` accessed on 09/21/2013.

[63] CMS Collaboration, "Search for the associated production of unparticles and a Z boson in pp collisions at $\sqrt{s} = 7\,\text{TeV}$ in the final state containing muons and missing transverse energy", *CMS Physics Analysis Summary* **CMS PAS EXO-11-043** (2011).

[64] CMS Collaboration, "Search for new physics in monojet events in pp collisions at $\sqrt{s} = 8\,\text{TeV}$", *CMS Physics Analysis Summary* **CMS PAS EXO-12-048** (2013).

Acknowledgement

Zu allererst möchte ich mich bei Prof. Hebbeker für die Möglichkeit bedanken, meine Diplomarbeit in einer großartigen Arbeitsgruppe am III. Physikalischen Institut A schreiben zu können. Es war eine einmalige Erfahrung, die Kollaboration an einem der größten internationalen Experimente hautnah kennenzulernen.

Für die Betreuung während meiner Zeit am Institut, bedanke ich mich herzlich bei Arnd Meyer. Dem wechselnden Personal im MUSiC-Büro gebührt mein Dank für seine Gastfreundschaft und ein angenehmes Arbeitsumfeld. Auch allen weiteren Kollegen, die immer für Diskussionen und Fragen aller Art zur Verfügung standen und an der Entwicklung der gemeinsam genutzten Software teilhaben, spreche ich an dieser Stelle meinen Dank aus. Insbesondere möchte ich Klaas Padeken erwähnen, der mir als Experte bei den spezielleren Fragestellungen jederzeit hilfreiche Tipps geben konnte. Zudem möchte ich den Korrekturlesern Prof. Hebbeker, Arnd Meyer und Michael Brodski für ihren Zeitaufwand und wertvolle Verbesserungsvorschläge danken.

Last but not least geht ein ganz besonderes Dankeschön an meine ganze Familie, die in allen Lebenslagen stets ein großer Rückhalt ist. Vor allem meine Eltern haben mit ihrer unermüdlichen Unterstützung dazu beigetragen, dass ich es auf meinem Lebensweg bis hierhin geschafft habe. DANKE!!!

Ich versichere, dass ich die Arbeit selbstständig verfasst und keine anderen als die angegebenen Quellen und Hilfsmittel benutzt sowie Zitate kenntlich gemacht habe.

Aachen, den 02.10.2013

Lars Reusch